NON-IDEAL MAGNETOHYDRODYNAMICS OF SELF-GRAVITATING FILAMENTS

Magnetohidrodinámica no ideal de filamentos auto-gravitantes

Por: Nicol Gutiérrez Vera

Tesis presentada a la Facultad de Ciencias Físicas y Matemáticas de la Universidad de Concepción para optar al grado académico de Magíster en Ciencias con Mención en Física

Marzo 2022

Concepción, Chile

Profesor Guía: Dr. Stefano Bovino
Comisión: Dr. Stefano Bovino, Dr. Tommaso Grassi, & Dr. Dominik R.G. Schleicher

Para toda mujer en STEM: sí se puede.

AGRADECIMIENTOS

I would like to thank my guide professor, Prof. Dr. Stefano Bovino, for all the patience and support in this Master's work. Thanks for teaching me, for putting your confidence in me and giving me this amazing topic to work in, and for introducing me to the collaborators for which this Thesis is possible: Dr. Tommaso Grassi, Dr. Alessandro Lupi, and Dr. Daniele Galli. Thanks to my co-guide and collaborator, Prof. Dr. Dominik Schleicher, for being so careful and nice to me, for taking your time to help me with any question I had.

Agradezco a mi madre y mi padre, Verónica y Jorge, por no haber dudado de mis capacidades, de darme el apoyo incondicional desde aquel día en mi adolescencia que les dije que quería ser astrónoma y no desanimarme, de darse el tiempo para poder comprender qué es lo que hago y qué me apasiona, sobre todo a mi madre por mostrarme la capacidad infinita de las mujeres. Agradezco a mis amigas de la vida: Brenda, Natalia y Nayarette por siempre estar ahí, a mis amigos y amigas de la universidad por toda la ayuda, sobre todo a aquellos con quienes pasamos estos años de postgrado más complejos y nos apoyamos entre nosotros. Gracias Camila y Philipe por enseñarme a que sí puedo trabajar en grupo y disfrutarlo, gracias Andrea por tu ayuda desinteresada. Gracias a Danilo, por abrirme los ojos y hacerme reconocer mis virtudes, por ser el pilar fundamental de mi desarrollo en toda mi etapa universitaria y celebrar mis logros como si fueran suyos. Y no menos importante, a mis perritas Alice y Bombón, por darme la serotonina para seguir.

Resumen

En el estudio de la formación estelar, las nubes moleculares son objetos importantes debido a que en ellas, las estrellas tienen cabida a su formación. Diversos estudios observacionales han encontrado estructuras filamentosas que hoy en día llamamos filamentos, y conocemos perfectamente su importancia dentro del proceso de formación estelar gracias a simulaciones numéricas. Sin embargo, los trabajos computacionales dificilmente agregan ingredientes importantes como son los campos magnéticos y efectos no-ideales, y química. Algunos de estos trabajos han investigado por separado cómo la química, efectos difusivos, campos magnéticos y su estructura impactan la dinámica del gas, denotando el papel clave que tienen estos parámetros.

Motivados por estos resultados, investigamos cómo la magnetohidrodinámica (MHD) no ideal combinada con un modelo químico simplificado, afectan la evolución y acreción de un filamento. Para esto, presentamos un modelo de un filamento auto-gravitante, turbulento y que acreta material, usando LEMONGRAB, un código uni-dimensional (1D) de MHD no ideal que incluye química. Exploramos la influencia de la MHD no ideal y parámetros tales como la orientación y magnitud del campo magnético, taza de ionización por rayos cósmicos, entre otros, en la evolución del filamento, anchura y taza de acreción. Hemos encontrado que la anchura y taza de acreción del filamento son determinados por las propiedades del campo magntético, incluyendo la magnitud inicial y su orientación con respecto a la dirección del flujo de acreción, y el acoplamiento con el gas, controlado por la taza de ionización de rayos cósmicos. Aumentar la taza de ionización de rayos cósmicos conlleva a un menor comportamiento no ideal, disminuyendo el soporte de presión magnética, y por ende, amortiguando la eficiencia de acreción con un consecuente ensanchamiento del filamento. Por la misma razón, hemos obtenido anchuras más estrechas y mayores tazas de acreción cuando se reduce la magnitud inicial del campo magnético. En general, mientras estos factores afectan los resultados finales por un factor de ~ 2, eliminar la MHD no ideal resulta en variaciones mucho mayores (sobre un factor ~ 7). Estos resultados ponen en evidencia que la inclusión de efectos de MHD no ideal y rayos cósmicos son cruciales para el estudio de filamentos auto-gravitantes y en determinar cantidades observables cruciales, como la anchura y taza de acreción del filamento.

Abstract

In the star formation study, the molecular clouds are important objects as there is where the stars form. Diverse observational studies have found filamentary structure which today we call filaments, and we know their importance in the star formation process thanks to numerical simulations. However, the numerical works hardly add important ingredients as magnetic fields and non-ideal effects, and chemistry. Some of these works have separately investigated how chemistry, diffusion effects, magnetic fields and their structure impact the gas dynamics, denoting the key role that these parameters have.

Motivated by these results, we investigate how non-ideal magnetohydrodynamic (MHD) combined with a simplified chemical model affect the evolution and accretion of a filament. For this, we present a model of an accreting self-gravitating turbulent filament using LEMONGRAB, a one-dimensional (1D) non-ideal MHD code including chemistry. We explore the influence of non-ideal MHD and parameters such as the orientation and strength of the magnetic field, cosmic ray ionization rate, and others, in the evolution of the filament, width and accretion rate. We found that the filament width and the accretion rate are determined by the magnetic field properties, including the initial strength and its orientation with respect to the accretion flow direction, and the coupling with the gas controlled by the cosmic ray ionization rate. Increasing the cosmic rate ionization rate leads to a less non-ideal MHD behaviour, reducing the magnetic pressure support, and hence damping the accretion efficiency with a consequent broadening of the filament width. For the same reason, we obtain a narrower width and a larger accretion rate, when we reduce the initial magnetic field strength. Overall, while these factors affect the final results by approximately a factor 2, by removing the non-ideal MHD, it results in a much larger variation (up to a factor 7). These results put in evidence that the inclusion of non-ideal MHD effects and cosmic rays is crucial for the study of self-gravitating filaments and in determining critical observable quantities, like the filament width and accretion rate.

Keywords – star formation, filaments, methods: numerical, Magnetohydrodynamics (MHD)

Contents

Contents   v

List of Tables

List of Figures

Chapter 1

Introduction

1.1 Molecular clouds

Molecular clouds are the densest regions in the interstellar medium, formed mainly by molecular hydrogen H_2, with a typical temperature of 10-20 K. Most of the molecular gas in the Milky Way is distributed near the rotational plane, concentrated to inner regions in the "molecular ring" situated about 3-5 kpc from the center of the galaxy. Here stars are formed during the gravitational collapse of the cloud in the densest regions, the so-called "cores", condensations of molecular gas with densities larger than 10^4 cm^{-3}. The most abundant molecule after H_2 is carbon monoxide CO, which is the most common tracer of molecular gas, whose low rotational transitions lie between 4-22 K above the ground state. In the Milky Way, masses and sizes of molecular clouds are around $\sim 10^6 M_\odot$ and ~ 100 pc for giant molecular clouds to ≤ 10 $M_\odot$ and ≤ 1 pc and smaller. The lifetime of a cloud in the spiral arms of the Milky Way is limited to 10^8 years, and the duty cycle of the star formation within the cloud implies lifetimes lower than 30 Myr. Short lifetimes (a few Myr) mean that supersonic turbulence within a molecular cloud need not be regenerated, because clouds are dispersed rapidly.

Gravitational collapse plays an important role in star formation, which is affected by a complex interplay of physical and chemical processes. For a cloud with thermal support, the collapse happens when the mass exceeds the Jean mass M_J, dependent on the temperature T and the total particle density n. If there is no pressure support, collapse happens in a free-fall time t_{ff}, which is inversely

dependent on n. For example, for a typical cloud with $T = 10$ K and $n = 50$ cm^{-3}, $M_j \leq 80$ M$_\odot$ and $t_{ff} \leq 5 \times 10^6$ years. But we know that cloud lifetime is longer, this discrepancy leads us to consider turbulence and magnetic fields as important ingredients in regulating the star formation process.

The origin and nature of turbulence in molecular clouds is still an unsolved problem in the theory of star formation. Turbulent motions may promote star formation by collecting additional mass into limited regions, which could become gravitationally unstable and collapse, or inhibit star formation by providing a "pressure" which prevent the gravitational collapse. Small scale supersonic motions in gas produce shocks and dissipate energy. The interstellar turbulence is an agent that imposes order in the form of structures and correlation between various fields of the flows (Hennebelle and Inutsuka, 2019). On the other hand, the magnetic field strength tends to increase as the gas is compressed, acting against star formation. In addition, the material could accumulate along the field lines in the limit of the *flux freezing*, where inertia or even gravity can dominate the resisting magnetic forces and fold the field lines. The denser gas (with high pressure) where gravitational compression is higher can confine magnetic fields strongly, but a strong magnetic field can manage the compression and prevent it, hence in low dense regions the magnetic pressure overcome the ram-pressure. The magnetic critical mass M_Φ, which depend on the magnetic flux Φ_B, tells us if the magnetic forces can handle the gravitational collapse. As Φ_B does not change due to the flux freezing, neither M_Φ. When a cloud has $M > M_\Phi$, the magnetic force is unable to halt collapse and the cloud is called *magnetically supercritical*. For clouds with $M < M_\Phi$, gravity is weaker than the magnetism and the cloud is called *magnetically subcritical* (Evans II, 1999; Hartmann, 2009; Fukui and Kawamura, 2010; Crutcher, 2012; Heyer and Dame, 2015; Krumholz, 2015, and the references therein).

1.1.1 Thermodynamics of molecular clouds

Before going into the structures formed in the molecular clouds, we must ask ourselves what controls the temperature of molecular gas to know what will affect the structures in the cloud. We already said that the typical temperature of the clouds is about ~ 10 K, which is very low. For this, we must go into the heating and cooling processes in the molecular ISM.

1.1.1.1   Heating processes

The heating is produced when the kinetic energy is transfer from the species to the interstellar gas, principally by the removal of an electron from the specie by an energetic particle or photon, and the suprathermal electron produced heats the interstellar gas by thermalization though elastic collisions. Macroscopically, the heating is mainly hydrodynamical, as the gas can couple to the fluid movement. It can be produced by turbulence (shock waves), there is viscous heating (ambipolar diffusion), gravitational heating (compression), and mechanic heating due to stellar winds or supernovae explosion. In the other hand, microscopically it is due to the gas-grain interactions and gas-dust radiation (just if the dust is warmer than the gas), there is photo-electric heating (HI regions, cold diffuse ISM), photo-heating (HII regions), photo-ionization (dense region illuminated by strong FUV fields), chemical heating (exothermic process), high energy photons as X-rays ($T>10^6$K ISM from supernova remnants), and cosmic rays. Here, we will focus on the dominant process in the densest regions of molecular clouds.

While in the atomic ISM the grain photo-electric effect is the dominant heating process, the cosmic rays are able to penetrate the densest regions of molecular clouds due to the low interaction cross-sections. This process starts with the interaction of a cosmic ray particle with an electron in the way that the electron is knocked from the molecule, e.g. with H_2:

$$CR + H_2 \rightarrow H_2^+ + e^- + CR. \tag{1.1.1}$$

But the electron cannot easily transfer directly its energy to other particles in the gas easily due to its low mass, most of the collisions are elastics and the energy is not transferred to the impacted particle. However, the energy of the electron (typically $\sim$30 eV) is enough to ionize or dissociate other hydrogen molecules, which provides an inelastic reaction that can convert some of the CR's energy to heat. If the heat is due to dissociation, in which the electron strikes a H_2 molecule and dissociates it, any excess energy in the electron goes into kinetic energy of the two recoiling hydrogen atoms, and the atoms can share that energy with the rest of the molecular gas, as they are so massive in comparison to the electrons. Another possibility is that an electron hits the hydrogen molecule and excites it without dissociating it. The hydrogen molecule then collides with another

hydrogen molecule and due to this collision, de-excites, and the excess energy is shared. Finally, the cosmic ray can create a H_2^+ ion that undergoes chemical reactions with other molecules and release heat. This is chemical heating and there are a lot of possible exothermic reaction chains in which heavy ions are produced recoiling at high speeds and can share their energy via collisions.

1.1.1.2 Cooling processes

In the cooling processes the particles species take the energy from the gas, it mainly arises from collisional excitation where the energy is removed as a photon which leaves the gas cloud with spontaneous emission, or due to collisional ionization where an electron uses its energy to remove another electron from an atom. Recombination also produces cooling as the bounding and kinetic energy are irradiated. For the cooling, it is important to have a high frequency of collisions and high probability of energy exchange, the thermal energy of the gas must be higher than the exchanged energy, and the excitation energy be transported via photons.

When atoms, molecules or ions excited due to collisions transfer part of their kinetic energy in radiation we have the radiative cooling, and it depends on the density of the medium. This evolves electronic, rotational and vibrational transitions. Some of the most main coolants are CII and OI in neutral regions and for lower temperatures, only CII. OII, OIII, NII, NIII, NeII, NeIII for ionized regions, including the Lyman α (H) for temperatures above 10^4 K, and forbidden lines for temperatures lower than 10^4K (important in the warm neutral medium and cool neutral medium). In the other hand, the cooling also is produced due to the recombination of electrons on charged dust grains, where the cooling rate increases with increasing temperatures of grains. In Fig. 1.1.1 we show the thermal and chemical equilibrium state of a numerical model from Inoue and ichiro Inutsuka (2012) which represents warm atomic gas of T$\sim 10^4$ to cold molecular gas T~ 10 where main cooling and heating processes are presented.

The main cooling process in molecular clouds are molecular lines and dust radiation. As dust grains are solids, they are thermal emitters, but they are only able to cool the gas if collisions between dust grains and hydrogen molecules occur often enough to keep them thermally well-coupled, which is at densities around $10^4 - 10^5$cm^{-3}, higher than the typical density in a giant molecular cloud (GMC). The other
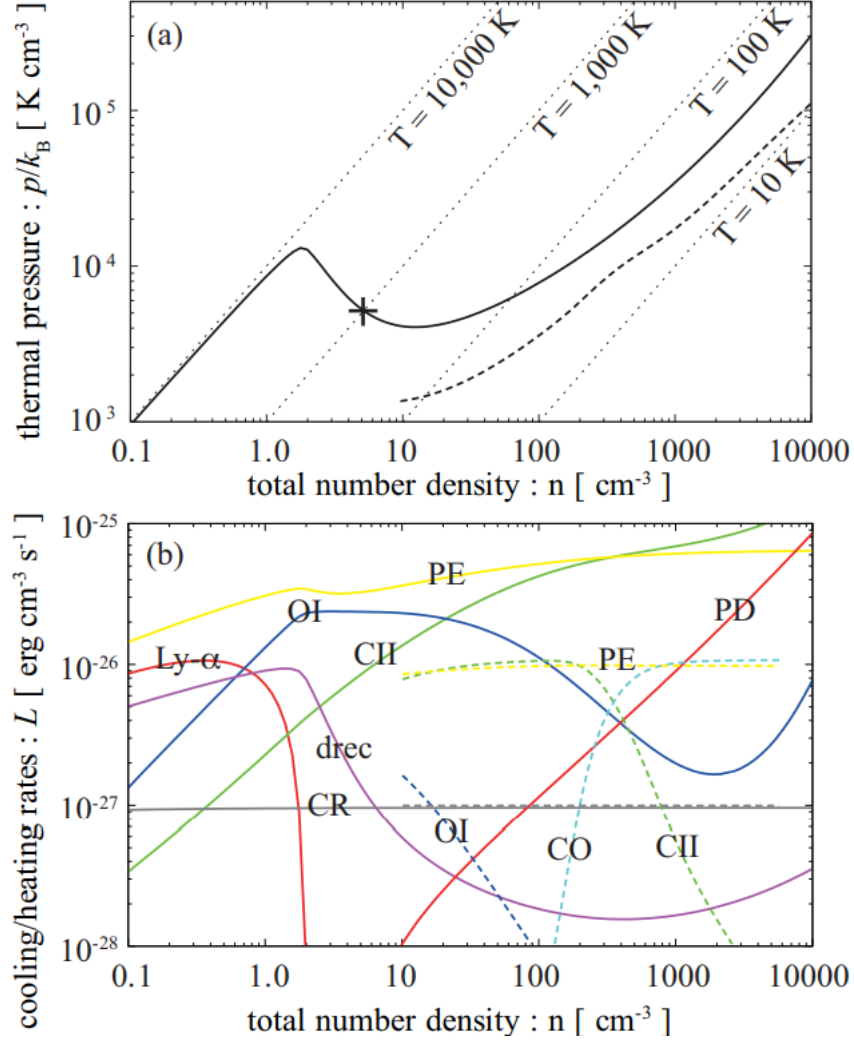
Figure 1.1.1: (a) Themal and chemical equilibrium state and (b) cooling and heating rates of the thermal and chemical equilibrium, both por Av=0 (solid) and Av=1 (dashed), from Inoue and ichiro Inutsuka (2012). In panel (a), the dotted lines are isotherms of T=$10^1, 10^2, 10^3$ and 10^4 K. In panel (b) Ly-α denotes Lyman α cooling, CII and OI are the fine structures transitions, DREC correspond to the recombination of electrons with grains and PAHs, CO denotes ro-vibrational cooling by CO molecules, PE is the photo-electric heating by PAHs, CR denotes the cosmic ray heating, and PD correspond to photo-dissociative heating of H$_2$ molecules.

process is line emission, in which the CO molecules and the CI fine structure play
a critical role. The CO molecules are excited by inelastic collisions with hydrogen
molecules, the collisions convert kinetic energy to potential energy within the
molecule. Then, the molecule could de-excites radiatively, the resulting photon
escapes the cloud, and the cloud loses energy and cools (Lequeux, 2005; Krumholz,
2015, and the references therein).

1.2   Filaments

Filamentary structures in molecular clouds (e.g., Ward-Thompson et al. 2010,
for the Polaris Flare cloud, Kirk et al. 2013, for the Taurus region, Alves de
Oliveira et al. 2014, for the Chamaeleon cloud complex) have been revealed by
Herschel observations (André et al., 2010; Molinari et al., 2010), suggesting that
prestellar cores may form from the gravitational fragmentation of marginally
supercritical and magnetized filaments (Könyves et al., 2015; Benedettini et al.,
2018), promoting star formation in dense gas (Bresnahan et al., 2018). The
filaments observed by *Hershel* share common properties, such as a central width of
$\sim 0.1 \pm 0.03$ pc (Arzoumanian et al., 2011), which may increase with the distance
above 300 pc from the observer (Panopoulou et al., 2021). This filamentary
structures are typically very long, about ~ 1 pc or more, nearly uni-directional,
and many of them appear co-linear to the major axis of the cloud in which they
live. Additional observations revealed a large-scale network of sub-filaments
connected to filamentary structures (e.g. Schneider et al., 2010, via IRAM 30m
and the Five College Radio Astronomy Observatory), aligned with the direction
of the magnetic field, which can represent a mass reservoir for further growth
of the filament and the cores embedded into it (André et al., 2014, and the
references therein).

If we refer to the possible formation of the filaments, how they growth and then
lead to star formation, we should talk about the accretion process. The accretion
is the accumulation of particles into a massive object, by gravitationally meaning.
Parameters as the Jeans length and Jeans mass can be a useful guide to know the
scales at which the instabilities can grow up and produce a mass concentration,
but Jeans criteria is useful only at small scales where gravitational collapse holds
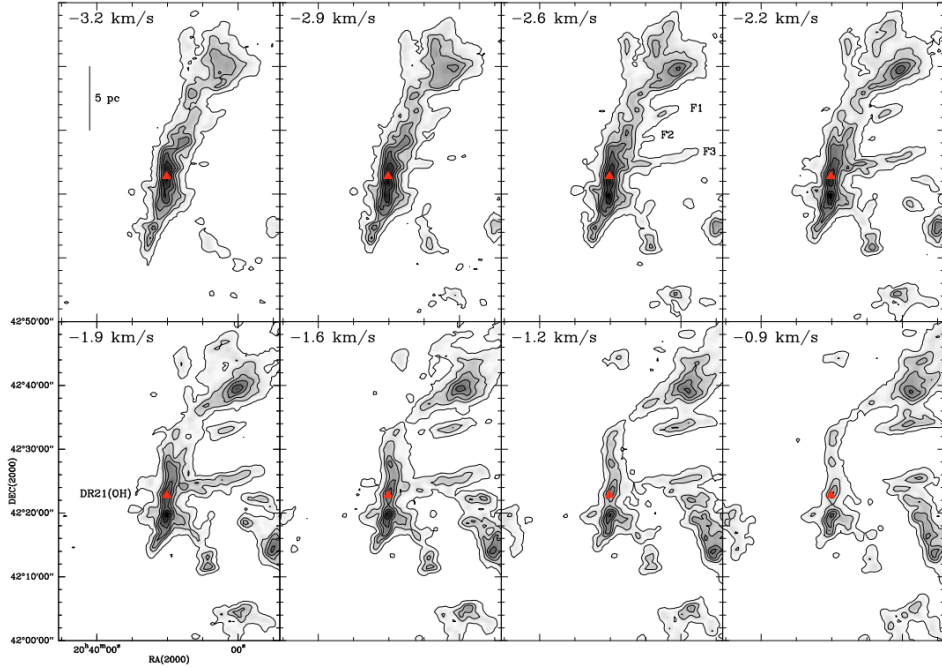
Figure 1.2.1: Channel maps of ^{13}CO 1→0 emission in Cygnus X North observed with the FCRAO from Schneider et al. (2010). F1, F2 and F3 correspond to the mayor sub-filaments connected to the DR21 filament.

and does not tell the characteristic masses at which the cloud could fragment. It can help us to know how do the filaments could be formed. Burkert and Hartmann (2004) examined the collapse of an elliptical sheet as the possible way filaments could form. The sheet piles up material at its edge until having extra concentrations of density at each end, then the collapse of the elongated sheet will produce a filament. For the fragmentation of the filament and the possible born of prestellar cores, André et al. (2010) propose that cores form according to complex networks of long, thin filaments that form first within molecular clouds, and then go through fragment into a number of prestellar cores. For filaments formed in a turbulent interstellar medium and aligned with the magnetic field, Xu et al. (2019) studied dust extinction maps of molecular clouds in the Gould Belt and show that when the magnetic field is perpendicular to the cloud, the filament shows a more uniform distribution of mass and affect the fragmentation process. This is consistent with the magnetic fields perpendicular to clouds can prevent the cloud-fragmentation more efficiently, giving as result a lower star formation efficiency.

The evidence of core growth in filaments leads to speculate that this process occurs primarily through filamentary accretion. Numerical works of gravitational collapse in turbulent magnetized regions (Balsara et al., 2001) showed that the filaments are linked to the high-density cores, and that material accretion onto the cores is channeled along with the magnetized filamentary structures. Thus, Balsara et al. postulate that this mechanism of accretion along filaments may provide a means for molecular cloud cores to grow to the point where they become gravitationally unstable and collapse.

1.2.1   Magnetic fields and non-ideal effects

The role of the magnetic field in the star-formation process and particularly of its orientation with respect to the filament axis has been widely discussed (Soler et al., 2013; Planck Collaboration et al., 2016b) and represents a crucial point to understand how the cores embedded in the filament grow in mass and trigger the formation of protostellar objects. Observational data from Zeeman surveys (Crutcher, 2012) and two-fluid simulations (Inoue et al., 2007) show that the maximum strength of the interstellar magnetic field is $\sim 10~\mu$G for gas with densities below $n_{\rm H} \sim 300$ cm^{-3}, increasing significantly at higher densities. This is determined by the balance between ambipolar diffusion and the accumulation of the magnetic field due to condensation. The comparison between purely three-dimensional hydrodynamical models and magneto-hydrodynamics (Hennebelle and Audit, 2008) shows that magnetic fields have a strong influence on the filamentary structure. On the other hand, the magnetic field can suppress fragmentation within filaments (Kirk et al., 2015; Tilley and Pudritz, 2007).

Polarisation measurements often show that the orientation of the magnetic field is nearly perpendicular to the major axis of the star-forming filament, but aligned with low-density filamentary structures sometimes called "striations" (Planck Collaboration et al., 2016a), a result also found in numerical simulations (e.g., Nakamura and Li, 2008). Padoan and Nordlund (1997) showed that during the formation of filaments, the compression due to the super-Alfvénic turbulence results in a parallel orientation of the magnetic field to the elongated structures. Cox et al. (2016) analyzed the filamentary structure of Musca, differentiating the main filament and the striations close to it, showing that they are parallel to the plane-of-the-sky local magnetic field and quasi-perpendicular to the main

filament. On the other hand, Seifried and Walch (2015) found that the observed typical filament width of 0.1 pc (Arzoumanian et al., 2011) can be explained if the magnetic field is oriented along the major axis of the filament.

However, ideal magnetohydrodynamics may not be sufficient to study filaments, due to the impact of ambipolar diffusion and other non-ideal processes (Grassi et al., 2019). Indeed, the molecular clouds are weakly ionized, which means that the interaction between charges and neutrals become important in these regions. The ambipolar diffusion or the so-called ion-neutral drift takes an important part in the star formation process. The slippage of neutral species in a plasma concerning an internal magnetic field is the ambipolar diffusion and occurs when the ionization fraction is so low that collisions between neutral species and ions become rare, thus the neutral species moves relative to the ions, which moves tied to the magnetic field. This is a good approximation for molecular clouds and more for the ones which are dense enough to shield from the cosmic rays, or even for filaments. The ionization fraction drives the chemistry of molecular clouds and determines the strength of the coupling of the gas with the galactic magnetic field, modifying the gas dynamics. Cosmic rays ionize molecular clouds with a typical ionization rate of molecular hydrogen $\zeta_{\rm cr} \approx 10^{-16}$–$10^{-17}$ s^{-1} (Padovani et al., 2009; Padovani and Galli, 2011) and lead to ambipolar diffusion due to the interaction between neutral and charged particles and dust grains, in the presence of the magnetic field. The resistivity coefficient of ambipolar diffusion is dependent on the abundance of the ions (Grassi et al., 2019). Collisions between charged dust grains and neutral gas particles dominate the momentum transfer. Overall, the coupling between the magnetic field and the gas then depends on the density and the ionization degree (Shu, 1983).

1.2.2   Accretion onto filaments

As we said before, the accretion of filaments is important in the context of star formation, because it could play a key role in preventing dense filaments from collapsing to spindles, and to maintain constant inner widths while evolving (André, 2017). Some authors focused on different ways in which the ambient material could be accreted, considering the constraints imposed by the magnetic field direction inside molecular clouds. Based on *Herschel* observations, Shimajiri et al. (2019) showed that the accretion of ambient gas can be driven by the
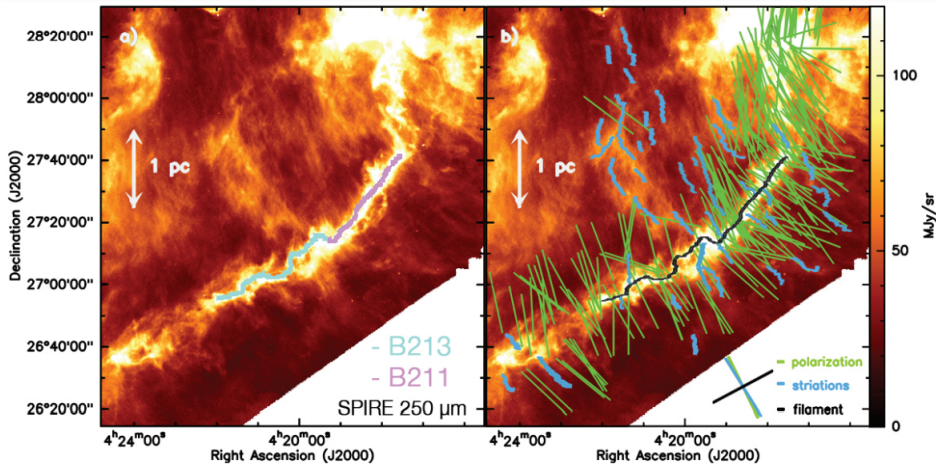
Figure 1.2.2: Herschel/SPIRE 250 μm image of the B211/B213/L1495 region in Taurus from Palmeirim et al. (2013). a) The light blue and purple curves show the crests of the B213 and B211 segments of the whole filament. b) Display of optical and infrared polarization vectors from Heyer et al. (2008), Heiles (2000), and Chapman et al. (2011) tracing the magnetic field orientation in the B211/L1495 region, overlaid.

gravitational potential of the filament. This provides a strong support for the scenario of mass accretion along magnetic field lines (oriented nearly perpendicular to the filament) proposed by Palmeirim et al. (2013) (see Fig. 1.2.2). Assuming a magnetic field perpendicular to the filament, Hennebelle and André (2013) considered radial accretion in a self-gravitating filament due to the combination of accretion-driven turbulence and dissipation of the turbulence by ion-neutral friction. Those mechanisms provide a reasonable explanation for the typical width of a self-gravitating filament. Finally, Gómez et al. (2018) proposed a "U"-shaped magnetic structure produced by dragging the field by the accretion flow, as shown in Fig. 1.2.3. In previous numerical works as Gómez and Vázquez-Semadeni (2014) a similar behaviour is shown when filaments are proposed as river-like flow structures, where the gas falling onto the filament changes the direction as the gas density increases, accreting mainly on the perpendicular direction with an accretion rate $\sim$30 $M_\odot$ Myr^{-1} pc^{-1}.
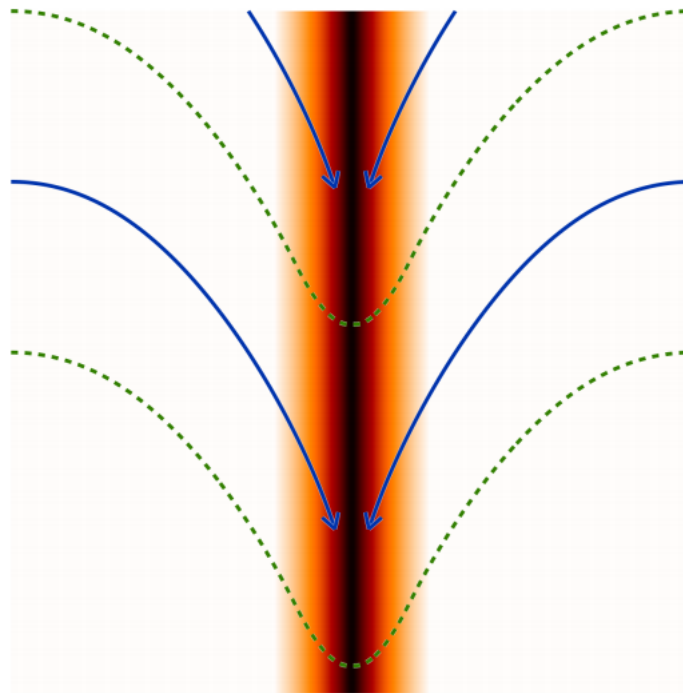
Figure 1.2.3: Sketch of the 'U'-shaped magnetic line geometry due to the accretion towards and along the filament from Gómez et al. (2018). Colours indicate the projected column density of the filament, solid lines show the flow of gas, dashed lines show the magnetic field lines, dragged by the accretion flow.

Chapter 2

Theorical framework

2.1   Non-ideal effects

When we refer to non-ideal effects, we must think to the generalized Ohm's law, which illustrates the balance between the acceleration of charged particles due to an electromagnetic field and the collisional drag with neutrals. The simplest case is when there is no magnetic field which could affect the trajectory of the charged particles and the currents are along the direction of the electric field. But the interesting case in which the magnetic field is not negligible shows us that the conductivity becomes a tensor on the contrary of the no-magnetic field case. This tensor produces the most important non-ideal effects in the non-ideal MHD: the Hall effect and ambipolar diffusion. In the following section we will explain how the ambipolar diffusion, ohm resistance, and Hall effect works.

2.1.1   Ambipolar diffusion

Charged species experiences the electromagnetic force directly, while the neutral species experiences the force through collisions with the charged species. The force experienced by the charged species is

$$\mathbf{F_L} = \frac{1}{4\pi}(\nabla \times \mathbf{B}) \times \mathbf{B}, \qquad\qquad (2.1.1)$$

which is the Lorentz force[1] and $\mathbf{B}$ is the magnetic field, while the neutral species experiences a relative drifts due to frictional force

$$\mathbf{F_d} = \rho_i \rho_n \gamma_{\mathrm{AD}}(\mathbf{v_i} - \mathbf{v_n}) \tag{2.1.2}$$

with γ_{AD} is the collisional coupling constant, being $\gamma_{\mathrm{AD}} \sim 3 \times 10^{13}$ cm^3 s^{-1} g^{-1} in ISM mixture (Draine et al., 1983), ρ_i, $\mathbf{v_i}$, ρ_n and $\mathbf{v_n}$ the ion and neutral density and velocity respectively. Here the drift velocity $\mathbf{v_d}$ (which is the effect of the ambipolar diffusion) can be computed as

$$\mathbf{v_d} \equiv \mathbf{v_i} - \mathbf{v_n} = \frac{1}{4\pi\gamma_{\mathrm{AD}}\rho_n\rho_i}(\nabla \times \mathbf{B}) \times \mathbf{B}. \tag{2.1.3}$$

This diffusion velocity affects the fluid when we write the equation of the evolution of the magnetic field (see Section 2.2), showing that the resisitivity produced by the ion-neutral drift is not-linear, but depends on $\mathbf{B}$ itself. The magnitude of the resistivity produced by ion-neutral drift is

$$\eta_{\mathrm{AD}} = \frac{|\mathbf{B}|^2}{\rho_i \rho_n \gamma_{\mathrm{AD}}}, \tag{2.1.4}$$

where $|\mathbf{B}|$ is the magnitude of the magnetic field vector.

2.1.2   Ohmic resistivity

The Ohmic diffusion originates from collisions between negative (electrons) and neutral particles. This diffusive term is the dominant non-ideal MHD effect only when the gas drag acting on the plasma particles is stronger than the Lorentz force acting on them. The diffusion coefficient is given by

$$\eta_{\mathrm{O}} = \frac{c^2 m_e \gamma_e \rho_n}{4\pi e^2 n_e}, \tag{2.1.5}$$

where c is the speed of light, m_e and n_e are the mass and number density of the electron, and γ_e is the rate coefficient of the collisional momentum transfer between electrons and neutrals, then, $\gamma_e \rho_n$ is the collision frequency of electrons with neutrals.

---

[1]Note that we work in CGS units, hence the presence of the 4π

2.1.3 Hall effect

The Hall effect is due to the drift between the positively and negatively charged particles (ions and electrons). Here, the magnetic diffusion coefficient is

$$\eta_{\mathrm{H}} = \frac{c|\mathbf{B}|}{4\pi e n_e}. \tag{2.1.6}$$

If we refer to the charged particles, i.e.: electrons, ions, charged grains, it becomes necessary to define the Hall parameter β_j (where j refer to the charged species) as the ratio between the gyro-frequency and the momentum exchange with the neutral species as

$$\beta_j \equiv \frac{|Z_j|e|\mathbf{B}|}{m_j c \gamma_j \rho}, \tag{2.1.7}$$

where $Z_j e$ is the charge of the respective species. With this parameter, we can measure how the species acts with respect to the neutrals and the magnetic field and characterize the direction of the drift of the particle. If $\beta_j \ll 1$ the drag force dominates over the Lorentz force and the neutral collisions decouple the particles from the magnetic field, but if $\beta_j \gg 1$ the specie is strongly tied to the magnetic fields. Ions are more massive than electrons, which means that $\beta_e \gg \beta_{\mathrm{ion}}$. Knowing this, if we assume that the charged particles correspond to ions and electrons, we can compare the magnetic diffusive terms and find the relations

$$\frac{\eta_{\mathrm{H}}}{\eta_{\mathrm{O}}} = \beta_e \quad , \quad \frac{\eta_{\mathrm{AD}}}{\eta_{\mathrm{H}}} = \beta_i, \tag{2.1.8}$$

where we can distinguish three diffusion regimes: i) $\beta_i \ll \beta_e \ll 1$, the medium is resistive as ions and electrons are coupled to the neutrals, so they are not affected by the magnetic field, then the ohmic resistivity is dominant, ii) $\beta_i \ll 1 \ll \beta_e$, the electrons are coupled to the magnetic field, but ions are not, which correspond to is the Hall effect, and iii) $1 \ll \beta_i \ll \beta_e$, where ions and electrons are coupled to the magnetic field and drift through the neutrals, the ambipolar diffusion. In the Eq. (2.1.3) if we ignore the constant values, β depends on the magnetic field magnitude and density (or number density n), Wardle (2007) shows the different regimes of $|\mathbf{B}|/\mathbf{n}$ illustrated in Fig. 2.1.1, note that ambipolar diffusion is dominant for lower n ($n_{\mathrm{H}} \sim 3 - 5$ cm^{-3}). Largest grains can not be described for Fig. 2.1.1,
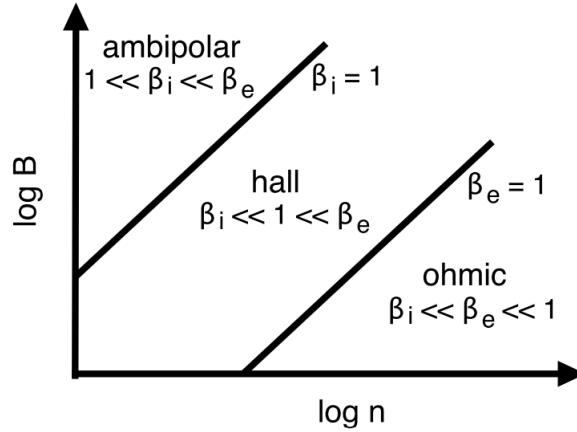
Figure 2.1.1: View of the magnetic diffusion regimes of a weakly-ionized plasma (Wardle, 2007).

if the majority of charged particles are tied to the neutrals the ohmic diffusion is dominant, ambipolar diffusion if are tied to the magnetic field, and Hall diffusion if are not tied to neutrals or the magnetic field.

2.2 Non-ideal magnetohydrodynamics equations

When a fully ionized plasma is treated as a single hydrodynamic fluid acted upon by electric and magnetic forces, it is called the 'magnetohydrodynamic' (or often abbreviated 'MHD') model. In principle, most of the astrophysical gas is almost fully ionized, so it works as a perfect conductor, which is known as a gas in *ideal* MHD limit. But molecular clouds are not very good plasmas ($\rho_n \approx \rho$ and $\rho_i \ll \rho_n$). The ion fraction is very low and the (cosmic ray) ionization rate is of the order $\zeta \sim 10^{-17}$ s^{-1}, the coupling of the gas with the magnetic field is imperfect, ions and neutrals do not move at exactly the same speed. The field follows the ions (less resistive) but neutrals are able to drift across the field lines, which means there is a slippage between ions and neutrals: ambipolar diffusion. A general description of these kinds of fluid starts with the mass conservation equation

$$\frac{\partial \rho}{\partial t} + \nabla \cdot (\rho \mathbf{v}) = \mathbf{0}, \tag{2.2.1}$$

where ρ is the mass density and $\mathbf{v}$ is the fluid velocity vector. The momentum conservation equation is described by

$$\rho\left(\frac{\partial \mathbf{v}}{\partial t} + \mathbf{v}\cdot\nabla\mathbf{v}\right) = -\nabla P + \frac{1}{4\pi}(\nabla\times\mathbf{B})\times\mathbf{B}, \qquad (2.2.2)$$

where $\mathbf{B}$ is the magnetic field vector and P is the total pressure. Additional non-electromagnetic forces may be included on the right-hand side of the equation, if necessary. The induction equation for the evolution of the magnetic field is

$$\frac{\partial \mathbf{B}}{\partial t} = \nabla\times\left(\mathbf{v}\times\mathbf{B} - \frac{\eta_{\mathrm{AD}}}{|\mathbf{B}|^2}(\nabla\times\mathbf{B})\times\mathbf{B}\right). \qquad (2.2.3)$$

For the total energy conservation equation

$$\frac{\partial E}{\partial t} = -\nabla\cdot\left\{(E+P)\mathbf{v} - \frac{\mathbf{B}}{4\pi}(\mathbf{B}\cdot\mathbf{v}) - \frac{\eta_{\mathrm{AD}}}{4\pi\mathbf{B}^2}(\mathbf{F_L}\times\mathbf{B})\right\} \qquad (2.2.4)$$

where E is the total energy, $\mathbf{F_L}$ the Lorentz force, and the last term of the right hand-side equation is the ambipolar electromagnetic force $\mathbf{E_{AD}} = (\mathbf{v_i} - \mathbf{v_n})\times\mathbf{B} = \mathbf{F_L}\times\mathbf{B}/\gamma_{\mathrm{AD}}\rho_i\rho_n$ (Masson et al., 2012). In this equation, the term accompanying η_{AD} illustrates the ambipolar diffusion heating of neutrals by ions (Shu, 1992). Finally, together with the magnetic field divergence (absence of magnetic monopoles),

$$\nabla\cdot\mathbf{B} = \mathbf{0} \qquad (2.2.5)$$

completes the non-ideal MHD equations for a molecular cloud type environment. This equation can be modified to describe the specific ambient we need to study.

Chapter 3

Metodology

Here, we report the numerical method and initial conditions employed in this work.

3.1 Numerical framework

To study the evolution of the filament we employ the LEMONGRAB code (Grassi et al., 2019), a 1D, non-ideal MHD code that solves the non-ideal MHD equations, with the aim of exploring how different micro-physics processes affect the evolution of density (ρ), temperature (T), magnetic field (B_i), energy ($\mathcal{E}$), and mass fractions of chemical species (ρX_i) in a controlled environment. The code also includes cooling/heating processes and grain chemistry (including charged grains). For the purpose of this study, we have coupled self-gravity to LEMONGRAB.

Given the dimensionality of the code, which implies $\partial_y = \partial_z = 0$, and the solenoidal condition that requires $\partial_x B_x = 0$, the coupled equations can be written as

$$\partial_t \rho = -\partial_x[\rho v_x], \tag{3.1.1}$$

$$\partial_t[\rho v_x] = -\partial_x\left[\rho v_x^2 + P^* - \frac{B_x^2}{4\pi}\right] - \rho\partial_x\Phi, \tag{3.1.2}$$

$$\partial_t[\rho v_y] = -\partial_x\left[\rho v_x v_y - \frac{B_x B_y}{4\pi}\right], \tag{3.1.3}$$

$$\partial_t[\rho v_z] = -\partial_x\left[\rho v_x v_z - \frac{B_x B_z}{4\pi}\right], \tag{3.1.4}$$

$$\partial_t B_x = 0, \tag{3.1.5}$$

$$\partial_t B_y = -\partial_x\left[v_x B_y - v_y B_x + \frac{\eta_{\mathrm{AD}}}{|\mathbf{B}|^2}(F_{B,x}B_y - F_{B,y}B_x)\right], \tag{3.1.6}$$

$$\partial_t B_z = -\partial_x\left[v_x B_z - v_z B_x + \frac{\eta_{\mathrm{AD}}}{|\mathbf{B}|^2}(F_{B,z}B_x - F_{B,x}B_z)\right], \tag{3.1.7}$$

$$\begin{aligned}\partial_t \mathcal{E} = \ &\Gamma_{\mathrm{cr}} - \Lambda - \rho v_x\partial_x\Phi - \partial_x\left\{(\mathcal{E} + P^*)v_x - \frac{B_x}{4\pi}(\mathbf{v}\cdot\mathbf{B})\right.\\ &-\frac{\eta_{\mathrm{AD}}}{\pi|\mathbf{B}|^2}[(F_{B,z}B_x - F_{B,x}B_z)B_z\\ &\left.-(F_{B,x}B_y - F_{B,y}B_x)B_y]\right\}, \end{aligned} \tag{3.1.8}$$

$$\partial_t(\rho X_i) = -\partial_x(\rho X_i v_x) + \mathcal{P}_i - \rho X_i \mathcal{L}_i. \tag{3.1.9}$$

In the above equations, Φ is the gravitational potential, $|\mathbf{B}|$ is the modulus of the magnetic field, Λ is the cooling rate, Γ_{cr} is the cosmic ray heating, ζ_{cr} is the cosmic ray ionization rate, and $\mathcal{P}_i$ and $\mathcal{L}_i$ are the production and loss terms of the i-th chemical species.

The total pressure $P^\star$ is

$$P^\star = P + \frac{|\mathbf{B}|^2}{8\pi}, \tag{3.1.10}$$

while assuming an ideal equation of state for the thermal pressure

$$P = (\gamma - 1)\left(E - \frac{\rho|\mathbf{v}|^2}{2} - \frac{|\mathbf{B}|^2}{8\pi}\right), \tag{3.1.11}$$

and related to the temperature T via the ideal gas law

$$P = \frac{\rho k_B}{\mu m_p}T, \tag{3.1.12}$$

where k_{B} the Boltzmann's constant, γ the adiabatic index, m_{p} the proton mass, and μ the mean molecular weight.

The Lorentz force components are

$$F_{B,x} = -B_y \cdot \partial_x B_y - B_z \cdot \partial_x B_z, \tag{3.1.13}$$

$$F_{B,y} = B_y \cdot \partial_x B_x, \tag{3.1.14}$$

$$F_{B,z} = B_z \cdot \partial_x B_x. \tag{3.1.15}$$

The ambipolar diffusion resistivity is given by

$$\eta_{\mathrm{AD}} = c^2 \left(\frac{\sigma_{\mathrm{P}}}{\sigma_{\mathrm{P}}^2 + \sigma_{\mathrm{H}}^2} - \frac{1}{\sigma_{||}} \right), \tag{3.1.16}$$

where σ_{P}, σ_{H}, and $\sigma_{||}$ are the Pedersen, Hall and parallel conductivities which are

$$\sigma_P = \frac{c}{B} \sum_i \frac{q Z_i \rho_i}{m_i} \frac{\beta_{i,n}}{1 + \beta_{i,n}^2}, \tag{3.1.17}$$

$$\sigma_H = \frac{c}{B} \sum_i \frac{q Z_i \rho_i}{m_i} \frac{1}{1 + \beta_{i,n}^2}, \tag{3.1.18}$$

$$\sigma_{||} = \frac{c}{B} \sum_i \frac{q Z_i \rho_i}{m_i} \beta_{i,n}, \tag{3.1.19}$$

where q is the elementary charge, m_i in the mass of the charged particle, $q Z_i$. ρ_i is the charge and density of the particle, respectively, and $\beta_{i,n}$ is the Hall parameter which take into account the interaction between charged and H_2 (the neutral specie used here). The sum is over the electrons, cations, and charged dust grains. The Hall parameter mentioned before, for collision between the ith charged particle and the neutral specie is

$$\beta_{i,n} = \left(\frac{q Z_i B}{m_i c} \right) \frac{m_i + m_n}{\rho_n R_{i,n}(T)}, \tag{3.1.20}$$

where ρ_n is the neutral gas mass density, m_n its mass, and $R_{i,n}(T)$ is the momentum exchange rate coefficient.

3.1.1   Addition of self-gravity

Given the spatial discretisation of the code, the Poisson equation can be easily discretised over the 1D grid at second-order via central differencing, as

$$\partial_x^2 \Phi \approx \frac{\Phi_{i+1} - \Phi_i + \Phi_{i-1}}{\Delta x^2} = 4\pi G \rho_i, \tag{3.1.21}$$

where Φ_i and ρ_i are the gravitational potential and density of the i-th cell (ranging from 1 to N, with N the number of resolution elements in the simulation), and Δx the spatial resolution of the simulation. For the boundary cells, we have included different boundary conditions (periodic, Dirichlet, or outflowing) among which the user can arbitrarily choose, although in this work we only consider periodic ones, i.e. $\Phi_1 = \Phi_N$. The potential is then calculated via matrix inversion, and the gravitational acceleration is finally obtained via central differencing as

$$g_x = -\partial_x \Phi \approx -\frac{\Phi_{i+1} - \Phi_{i-1}}{2\Delta x}. \tag{3.1.22}$$

3.1.2   Cooling and heating functions

The cooling function employed here depends on both temperature and number density. It corresponds to collisional-ionisation-equilibrium conditions typical of the interstellar gas, and has been derived with CLOUDY (Ferland et al., 1998) and tabulated by Shen et al. (2013). For this, we interpolate the data with the temperature and number density from the code (see Fig. 3.1.1) and impose a temperature floor of 10 K.

The heating function due to the cosmic rays is modeled as

$$\Gamma_{CR} = \zeta Q(n_H) n(H_2) \text{ erg cm}^{-3} \text{ s}^{-1}, \tag{3.1.23}$$

where ζ is the cosmic ray ionization rate, n_H is the number density of H nuclei, with $n_H = 2n_{H_2}$ in our chemical network, and $Q(n_H)$ is the heat deposited in the gas per ionisation event (Galli and Padovani, 2015).
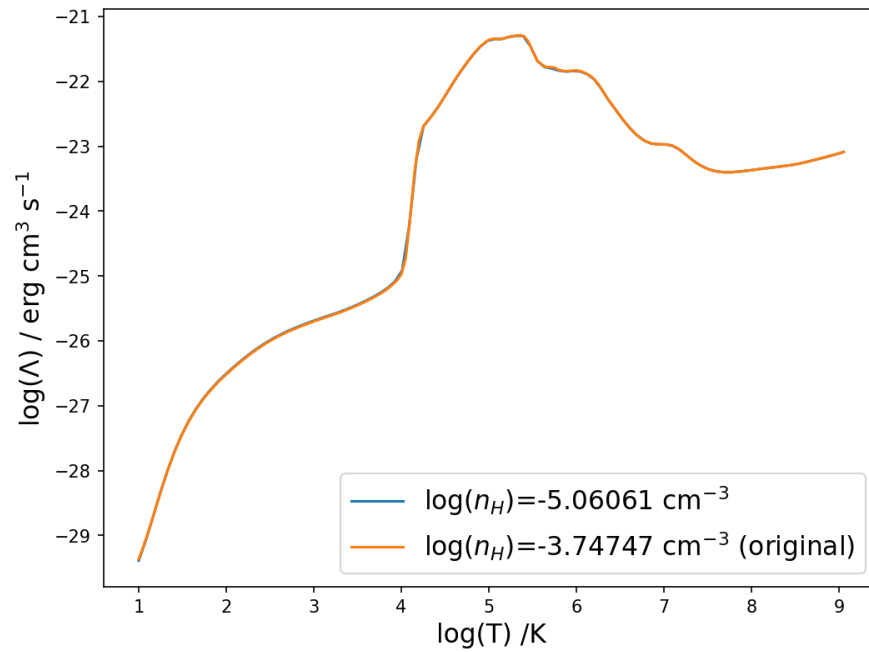
Figure 3.1.1: Interpolation of the (metal) cooling function from Shen et al. (2013) with temperature values from the code.
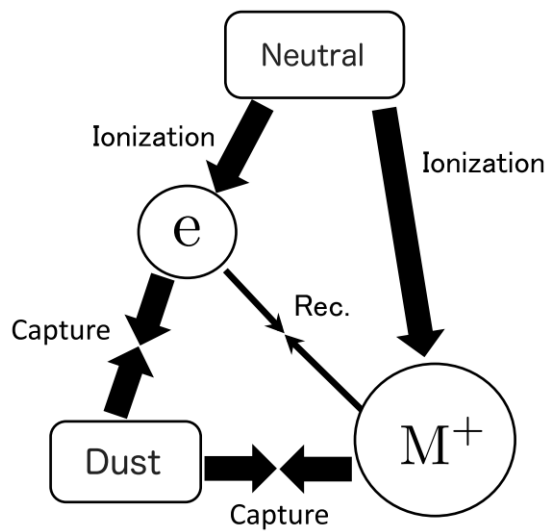
Figure 3.1.2: Scheme of the cascade reaction. M$^+$ Neutral gas is ionized by the ionization source, charge transfer is so fast that dissociative recombination and capture by dust is grain can be ignored (Fujii et al., 2011).

3.1.3   Chemical model

For this work, we employ the reduced chemical network of Grassi et al. (2019),
including 8 species: electrons e^-, X, X^+, and neutral and charged grains, i.e. g,
g^+, g^{++}, g^-, g^{--}; The species X and X^+ are a proxy of all neutral and cations
produced by a chain of fast reactions following H_2 ionization. Fujii et al. (2011)
explain show the reaction works as follows: when hydrogen molecules (being the
neutral specie) are ionized (by the cosmic rays, in our case) the resulting ion H_2^+
immediately reacts with H_2 to produce H_3^+, which reacts with other molecules to
leads heavier molecular ions. These ions are quickly destroyed by charge exchange
with atomic heavy metals (as Mg) leading to heavy metal ions (as Mg^+). As the
timescale of charge transfer is so short, dissociative recombination and capture of
molecular ions by dust grains can be neglected, and we treat the reaction as if the
heavy metal ions are formed directly by primary ionization (see Fig. 3.1.2).

We assume that the mass of X is the same as the mass of H_2, and the dust grains
rates are weighted, assuming an MRN distribution (Mathis et al., 1977) with the
same characteristics as in Grassi et al. (2019).

The differential equations for the production and loss rate, $\mathcal{P}_i$ and $\rho X_i \mathcal{L}_i$,
respectively, of the ith species are defined by

$$\mathcal{P}_i = m_i \rho^2 \sum_{r_1,r_2} k_{r_1,r_2} \frac{X_{r_1}}{m_{r_1}} \frac{X_{r_2}}{m_{r_2}}, \qquad (3.1.24)$$

$$\rho X_i \mathcal{L}_i = X_i \rho^2 \sum_{r_1} k_{r_1} \frac{X_{r_1}}{m_{r_1}}, \qquad (3.1.25)$$

where k_{r_1,r_2} is the reaction rate coefficient between species r_1 and r_2, while m_i and
X_i are the mass and the mass fraction of the ith specie. Both equations 3.1.24
and 3.1.25 conserve the total number density, but not the total mass as the H_2
molecule is converted into an Mg^+ atom, which is almost 24 times more massive.
To avoid this problem, the mass of Mg^+ is defined as $m'_{Mg^+} = m_{H_2} - m_{e^-}$.

3.1.3.1   Grain chemistry

Dust grains can recombine with electrons and exchange charge with cations
and amongst themselves (see Tab. 2 from Grassi et al., 2019). The grain size
distribution $\varphi(a)$ is integrated over the size range $a_{\min}$ to $a_{\max}$ to provide averaged

reaction rate coefficients, $k(a, T)$, which are a function of the grain size a:

$$\langle k(T) \rangle = \frac{\int_{a_{\min}}^{a_{\max}} \varphi(a) k(a, T) \mathrm{d}a}{\int_{a_{\min}}^{a_{\max}} \varphi(a) \mathrm{d}a} \tag{3.1.26}$$

for particle-grain interactions, and

$$\langle k(T) \rangle = \frac{\int_{a_{\min}}^{a_{\max}} \int_{a_{\min}}^{a_{\max}} \varphi(a) k(a, a', T) \mathrm{d}a \varphi(a') \mathrm{d}a'}{\int_{a_{\min}}^{a_{\max}} \int_{a_{\min}}^{a_{\max}} \varphi(a) \mathrm{d}a \varphi(a') \mathrm{d}a'} \tag{3.1.27}$$

for grain-grain interactions, where $k(a, a', T)$ are the rate coefficient for collisions of grains with radius a and a', respectively

3.2 Initial conditions

Our model consists of a self-gravitating turbulent filament with 0.1 pc width in a 2 pc size periodic box sampled with 1024 cells, which can accrete mass from both sides of the x-axis, i.e., the dimension on which the hydrodynamic equations are solved. It is important to clarify that the selected periodic boundary condition after test outflow and Dirichlet. Indeed, the outflow conditions cause high velocities at the boundaries because the cells do not have any gravitational pull from outside the simulation box, and Dirichlet conditions produce some numerical oscillations on temperature and density near the boundaries of the box, which is caused by the arbitrary conditions outside the box. For our study, we model the filament as a non-uniform slab with an oblique magnetic field.

To model the filament we adopt a Plummer-like profile as shown in Arzoumanian et al. (2011), over the x-axis, given by

$$\rho(x) = \frac{\rho_{\mathrm{ridge}}}{[1 + (x/x_{\mathrm{flat}})^2]^{p/2}}, \tag{3.2.1}$$

where ρ_{ridge} is the central density of the filament, x_{flat} is the characteristic width of the flat inner plateau of the filament, and p is the typical exponent of the profile. For this study, we assume the same parameters as adopted by Körtgen et al. (2018), i.e. $p = 2$ and $x_{\mathrm{flat}} = 0.033$ pc, and we align the minor axis of the filament with the x-axis. We report in Fig. 3.2.1 a sketch of the filament setup.

The box is initialized with a uniform temperature of 15 K, and is filled with a low-
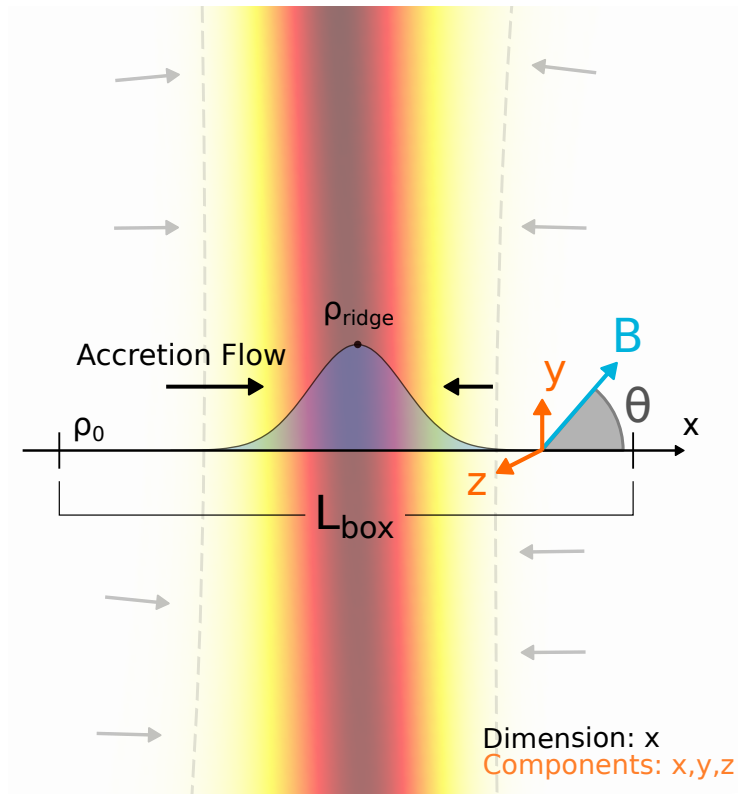
Figure 3.2.1: Representative sketch of our set-up. The code evolves 3 components $(x, y, z,)$ in a dimension (x), hence y and z have periodic boundary conditions. The x dimension traverses the filament (shaded gradient), and the initial density distribution along this component follows a Plummer-like profile with maximum density ρ_{ridge} and background density ρ_0, see Eq. (3.2.1). The gas accretes along the same axis, as indicated by the arrows. Finally, we have $\theta = \arctan(B_y/B_x)$. Note that the color palette employed for the filament has only pictorial purposes.

density medium with $\rho_0 \sim 2 \times 10^{-21}$ g cm^{-3} outside the filament region, the latter modelled according to the Plummer-like profile in Eq. (3.2.1), where we set $\rho_{\text{ridge}} \sim 3 \times 10^{-19}$ g cm^{-3}. The mass-to-line ratio is calculated as $(M/L) = 3(M/L)_{\text{crit}}$ where $(M/L)_{\text{crit}} = 2c_s^2/G$ and $c_s = \sqrt{k_b T/m_p \mu}$, then $(M/L) =\sim 86$ M$_\odot$ pc^{-1}. The free-fall time of the filament, defined as

$$\tau_{\text{ff}} = \sqrt{\frac{3\pi}{32 G \rho_0}}, \qquad (3.2.2)$$

measured at the background, it corresponds to ~ 1.3 Myr, for the conditions considered here.

The filament is initialised in a turbulent state given by a Mach number $\mathcal{M} = 2$, following a Burgers-like power spectrum, as detailed in Bovino et al. (2019) (see also Körtgen et al., 2017). In order to guarantee that the randomness of the initial velocity field does not introduce any bulk motion of the filament relative to the box, we correct the initial conditions by subtracting the mean initial velocity, to avoid any net momentum that could produce a drift in the filament.

The cosmic ray ionization rate is assumed to be initially uniform at a value $\zeta_{\text{cr}} = 10^{-17}$ s^{-1}. We set the initial electron fraction to $f_i = n_{\text{e}^-}/n_{\text{H}_2} = 10^{-7}$ and the dust-to-gas mass ratio to $\mathcal{D} = 10^{-2}$, as reported in Tab. 3.2.1. The initial abundances for each species are defined as

$$\rho_{\text{H}_2} = \frac{\rho}{1 + \mathcal{D} + f_i(m_{\text{e}^-} + m_{\text{Mg}^+})/m_{\text{H}_2}}; \qquad (3.2.3)$$

$$\rho_{\text{e}^-} = f_i \rho_{\text{H}_2} \frac{m_{\text{e}^-}}{m_{\text{H}_2}}; \qquad (3.2.4)$$

$$\rho_{\text{Mg}^+} = f_i \rho_{\text{H}_2} \frac{m_{\text{Mg}^+}}{m_{\text{H}_2}}; \qquad (3.2.5)$$

$$\rho_{\text{g(Z=0)}} = \rho_{\text{H}_2} \mathcal{D}; \qquad (3.2.6)$$

$$\rho_{\text{g(Z}\neq 0)} = 0, \qquad (3.2.7)$$

which guarantees $\rho = \rho_{\text{H}_2} + \rho_{\text{e}^-} + \rho_{\text{Mg}^+} + \rho_{\text{g(Z=0)}}$ and charge conservation for the system.

Physical quantity	Numerical value	Units
ρ_{ridge}	3.424×10^{-19}	g cm^{-3}
x_{flat}	0.0333	pc
L_{box}	2	pc
T	15	K
$\mathcal{M}$	2	-
B_0	10	μG
$B_{x,0}$	2.25	μG
$B_{y,0}$	9.74	μG
B_z	0	μG
θ	77	deg
f_i	10^{-7}	-
ζ_{cr}	10^{-17}	s^{-1}
$\mathcal{D}$	10^{-2}	-

Table 3.2.1: Initial conditions for the filament setup.

3.2.1 Magnetic field orientation

The magnetic field **B** is set perpendicular to the z-axis and is tilted relative to the x-axis (the accretion flow direction) as shown in Fig. 3.2.1. Note that when $\theta = 0$ the configuration is parallel to the flow direction, while for $\theta = \pi/2$ the configuration is perpendicular to the flow. Nevertheless, in this study we refer to parallel or perpendicular respect to the flux direction as our study is 1D on the x-axis. Because of the solenoidal nature of the field, B_x remains constant throughout the box, whereas the y component of the field is assumed to scale as (Crutcher et al., 2010)

$$B_y = B_{y,0} \left(\frac{\rho}{\rho_0} \right)^k , \tag{3.2.8}$$

where $k = 0.5$, and $B_{y,0} \equiv B_0 \sin \theta$, with $B_0 = 10 \ \mu$G.

The angle of the magnetic field is calculated as

$$\theta = \arctan \left(\frac{B_y}{B_x} \right) , \tag{3.2.9}$$

where the angle θ is measured from the x-axis (the flow direction). Note that since B_x is constant by construction, θ also varies with ρ, indicating that θ in our initial conditions refers to $B_y = B_{y,0}$.

Chapter 4

Analysis

In this section we present the results of our simulations divided in four parts: first we discuss we present our reference model based on the initial conditions listed in Tab. 3.2.1, in Section 4.2 we change the orientation and strength of the magnetic field, separately, in Section 4.3 we consider different cosmic rays ionization rate, and finally, in Section 4.4 we explore the effect of other physical quantities such as the initial turbulence seed, Mach number, density regimes, and k exponent of the magnetic field– density relation, Eq. (3.2.8).

4.1   Reference case

Fig. 4.1.1 shows the evolution of density, temperature, velocity in the x-direction, total velocity, the y-component of the magnetic field, total magnetic field, Mach number, and mass flux as a function of the x-coordinate at three different times, for our reference case (Tab. 3.2.1). The same panels include a comparison with the ideal MHD case (dashed lines).

At early times, the density shows a peak with an initial maximum of about 3×10^{-19} g cm^{-3} (9×10^4 cm^{-3}) in the center, slightly increasing at later times. A peak above 100 μG is also seen in the total and y-component of the magnetic field, triggered by the increase in density. In the outer regions, at $0.1t_{\mathrm{ff}}$ the density is about 2×10^{-21} g cm^{-3} (6×10^3 cm^{-3}). Some fluctuations develop as a result of the initial turbulence in the velocity components. The initial turbulence affects the first stages of the simulation generating fluctuations in the magnetic field, velocity,
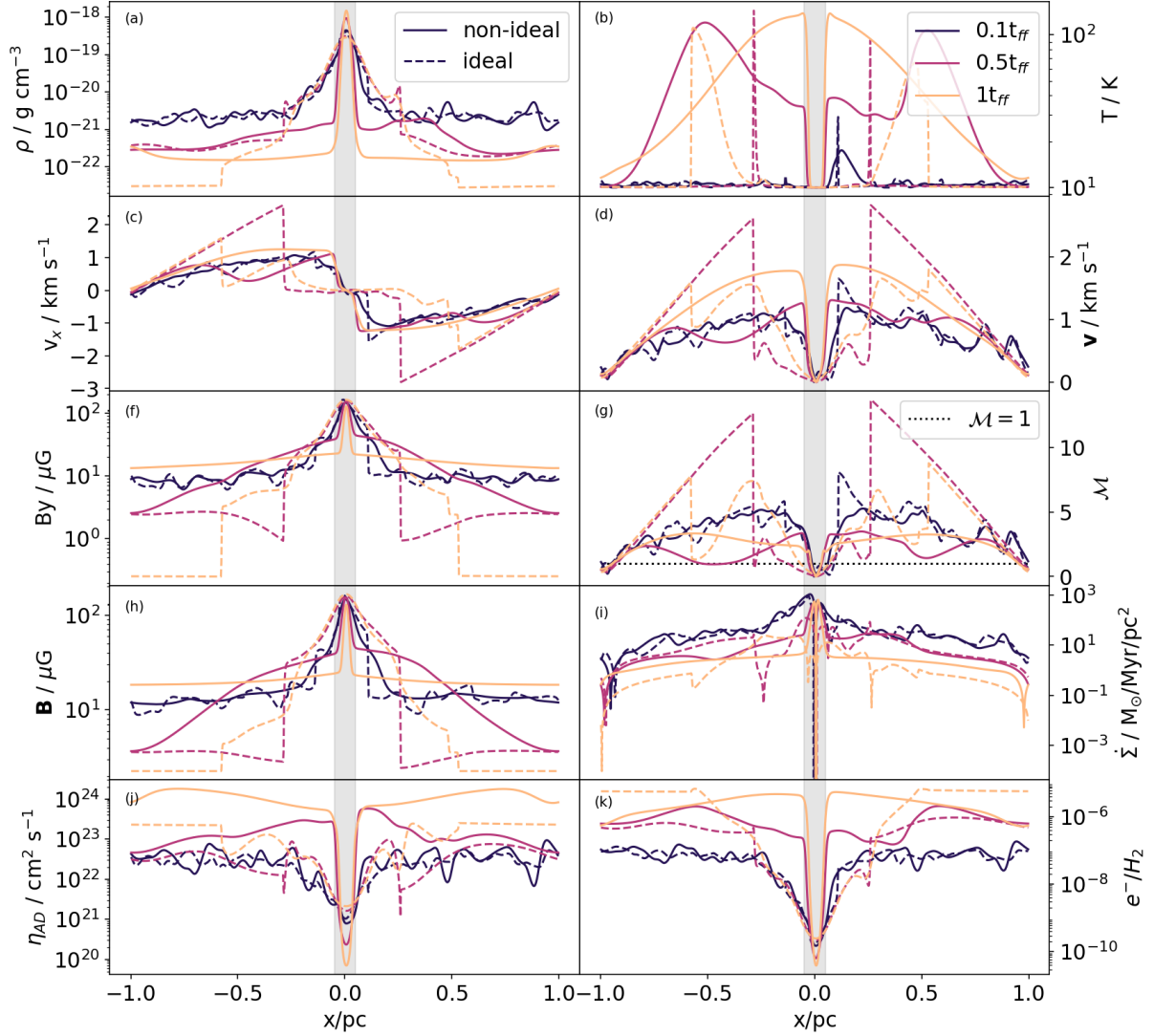
Figure 4.1.1: Profile along the x-axis of various physical quantities of the model at three different times: $t/t_{\mathrm{ff}} = 0.1$, 0.5 and 1.0. (a) density ρ, (b) temperature T, (c) x-component of the velocity v_x, (d) total velocity $\mathbf{v}$, (e) y-component of magnetic field B_y, (f) Mach number $\mathcal{M}$, (g) total magnetic field $\mathbf{B}$, (h) mass flux $\dot{\Sigma}$, (i) ambipolar diffusion resistivity coefficient η_{AD}, (j) abundance e^-/H_2. The solid lines correspond to non-ideal MHD, dashed lines to ideal MHD. The gray area in the middle corresponds to 0.1 pc to guide the reader to identify the typical width of the filaments.

and temperature, the latter showing values of ∼20 K. Both density and velocity profiles, after the initial stages, clearly show that a shock front is generated at around ±0.05 − 0.1 pc from the filament center; this represents the effective width of the filament.

From the velocity field we calculate the Mach number as $\mathcal{M} = v/c_s$, where $v = (v_x^2 + v_y^2 + v_z^2)^{1/2}$ is the total velocity magnitude, and $c_s = \sqrt{k_B T/\mu m_p}$ the sound speed, with k_B the Boltzmann's constant, T the gas temperature, m_p the proton mass, and μ the mean molecular weight. Similarly to the velocity field, the Mach number shows strong fluctuations at the first stages of evolution, going from values around 5 (highly supersonic) in the outer regions to $\mathcal{M} < 1$ (subsonic) in the center. The same behaviour is seen at later times.

From the density and the velocity field, we estimate the mass flux, reflecting the accretion flow in the x direction:

$$\dot{\Sigma} = \rho v_x\,. \qquad\qquad (4.1.1)$$

At early times, the mass flux shows peaks of $\sim 10^3$ M$_\odot$ Myr^{-1} pc^{-2} as a result of the density increase, which remains high also in the subsequent time-steps with a slight decrease.

The gravitational acceleration due to the mass accumulated in the filament leads to peak velocities up to 2 km s^{-1} moving inward, a velocity consistent with the expected free-fall time due to the available mass. The y- and z-components of the velocity (not shown), exhibit a similar behaviour to the x-component, but reach peak values of 1 km s^{-1} and 0.5 km s^{-1}, respectively; the latter close to the edges of the simulation box.

The thermal profile, after an initial isothermal state, shows three distinct regions: (i) the cold background gas at around 10 K, (ii) an efficient heating with temperature larger than 100 K produced by gas shocking, and (iii) the filament ridge where the high densities lead to efficient cooling, which brings the gas down to 10 K.

The x-component of the magnetic field remains constant in space and time by construction, while the z-component is initially zero because of the alignment, followed by fluctuations of a few μG due to the interaction with turbulence and

velocity fluctuations.

We note some differences from the ideal MHD case. In particular, the density peak tends to be broader due to the increased magnetic pressure and stronger coupling between the magnetic field and the density, while in the outermost parts the density tends to be lower than in the non-ideal MHD limit, just as the magnetic field. Due to the lack of non-ideal diffusivity, in the ideal MHD case there is no decrease of the peak of the magnetic field strength.

During the evolution, the density profile further steepens. At low densities, i.e. $\rho \lesssim 5 \times 10^{-20}$ g cm^{-3}, the electron fraction remains above 10^{-6}, but as the density approaches a maximum value of about 10^{-18} g cm^{-3}, the electron fraction drops to $\sim 10^{-10}$ due to efficient recombination. Despite the low electron abundance, the ambipolar resistivity decreases too, even at high densities. This is not surprising, because the highest densities reached in our model are around $n_\mathrm{H} \sim 10^5$ cm^{-3}, where electrons and X$^+$ are the dominant charge carriers, while grains take over at $n_\mathrm{H} > 10^8$ cm^{-3} (Marchand et al., 2016). At these higher densities, the abundance of electrons decreases due to dissociative recombination with X$^+$. Similarly, negatively charged grains recombine. The grain abundance (not shown) is strictly linked to the electrons here due to recombination; thus the evolution will be highly correlated. When the electron abundance drops off, the abundance of neutral and positively charged grains increases at high densities. Ambipolar diffusion keeps decreasing until the ion abundance increases enough for the diffusion with respect to the neutrals to become significant.

4.2   Magnetic field geometry and strength

To study how the initial geometry of the magnetic field influences the evolution of the filament, we test four different initial inclinations θ with respect to the x-axis, corresponding to $\theta = 5°$ (almost parallel to the flow), $\theta = 45°$, $\theta = 77°$ (reference case), and $\theta = 90°$ (perpendicular to the flow). In Fig. 4.2.1 and Fig. 4.2.2, the density, velocity and orientation angle of the magnetic field are shown at different times as a function of position. From now, we present the evolution of the model at two representative times: at half a free-fall time $0.5t_\mathrm{ff}$, and after one free-fall time $1.0t_\mathrm{ff}$. The central peak of the density and its width do not change very significantly for the different angles; However, when the magnetic field is closer to

Figure 4.2.1: Density and velocity along the x-axis for different initial angles. The solid line corresponds to the reference case. it Top panels: at $0.5t_{\mathrm{ff}}$; *bottom panels*: at $1.0t_{\mathrm{ff}}$.

Figure 4.2.2: Inclination of the magnetic field for the different initial angles. The solid line corresponds to the reference case. *Top panel*: $t = 0.5t_{\mathrm{ff}}$; *bottom panel*: $t = 1.0t_{\mathrm{ff}}$.

parallel to the gas flow, one expects that the gas flow to be is strongly impeded by the magnetic field. As a result, the density in the outer parts becomes even lower when θ is small, without changing significantly the density peak in the center, as the extra mass that is added to the center is very small. Similarly, the peak velocity increases as θ becomes aligned to the flow.

In general, the orientation of the magnetic field evolves both as a function of position and as a function of time. Particularly in the outer parts of the filament, the orientation angle decreases as a function of time, and the magnetic field tends to align with the flow of the gas. In the filament itself, on the other hand, the velocities are reduced due to increased thermal pressure, and the perpendicular component of the magnetic field is being compressed and amplified as more gas is accreted onto the filament. As a result, the orientation becomes closer to perpendicular within the dense component of the gas.

It is important to note that, because of the assumed symmetries, the simplified setup here may not necessarily hold in a realistic setting.

Nevertheless, what one can see clearly from Fig. 4.2.2 is the change of the angle of

the magnetic field between the outer parts and the inner parts of the filament. In a realistic setting, such a change of the angle may for instance correspond to a U-shape magnetic field as suggested by Gómez et al. (2018), or potentially other types of configurations that imply a change of the angle as a function of scale.

To study the effect of the magnetic field strength, we determine how the structure of the filament depends on four different initial field strengths, corresponding to 1×10^{-25} μG (no magnetic field), 5 μG (weak field), 10 μG (reference case) and 20 μG (strong field). The very weak magnetic field case is meant to essentially mimic a scenario without magnetic fields. In Fig. 4.2.3 and Fig. 4.2.4 the density, magnetic field angle and the x-velocity are shown as a function of position. The magnetic field strength drives the evolution of the filament. In particular, the strong magnetic field cases (10-20 μG) show a similar behavior, where the magnetic pressure support reduces the accretion velocity from the earlier stages (0.5 t_{ff}) as it counter-acts gravity, relatively broadening the density profile. On the other hand, the 5 μG case presents a similar evolution to the "no-B" case in the outer regions, and to the high B-cases in the inner part. At later stages, the former behavior is reduced, and the velocity profile globally follows the 10-20 μG cases. In these calculations, we assume an initial magnetic field angle of 77° as in the reference case. The direction of the weaker field becomes closer to be parallel to the flow in the ambient gas but close to perpendicular within the filament as in the previous simulation.

4.3   Cosmic rays ionization rate

To test the impact of the cosmic ray ionization rate (CRIR) on the evolution of the filament, we performed three simulations with $\zeta_{\mathrm{cr}} = 10^{-18}$ s^{-1} (low), 10^{-17} s^{-1} (reference) and 10^{-16} s^{-1} (high), respectively. The density, velocity, electron abundance, and ambipolar diffusion resistivity coefficient are shown in Fig. 4.3.1 and Fig. 4.3.2 for the different cases and at two different times. Higher cosmic-ray ionization rates produce an increase in the ionization fraction in the low-density accretion region (see Fig. 4.3.2 that corresponds to a stronger coupling between the gas and the magnetic field). As shown in Fig. 4.3.2, the lower electron density (left panels) corresponds to a less-ideal MHD, i.e., a higher ambipolar diffusion coefficient (right panels), determining a direct relation between CRIR and non-
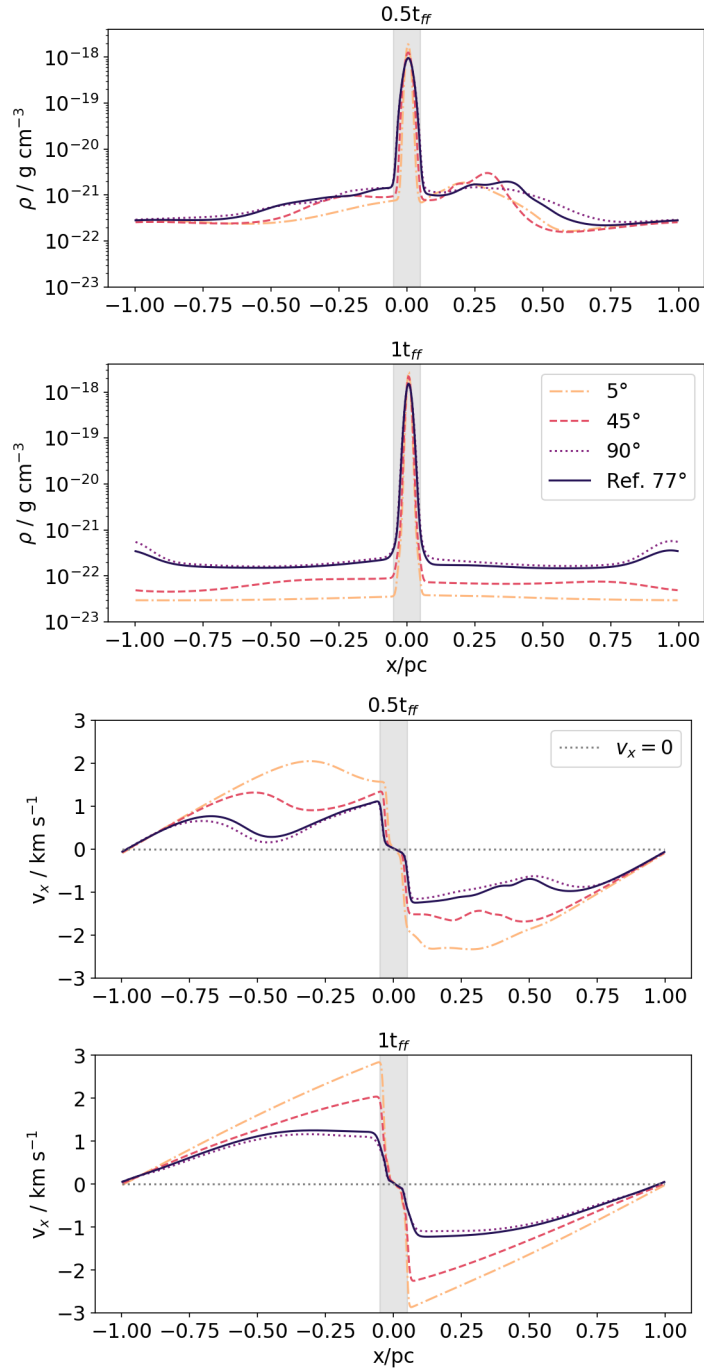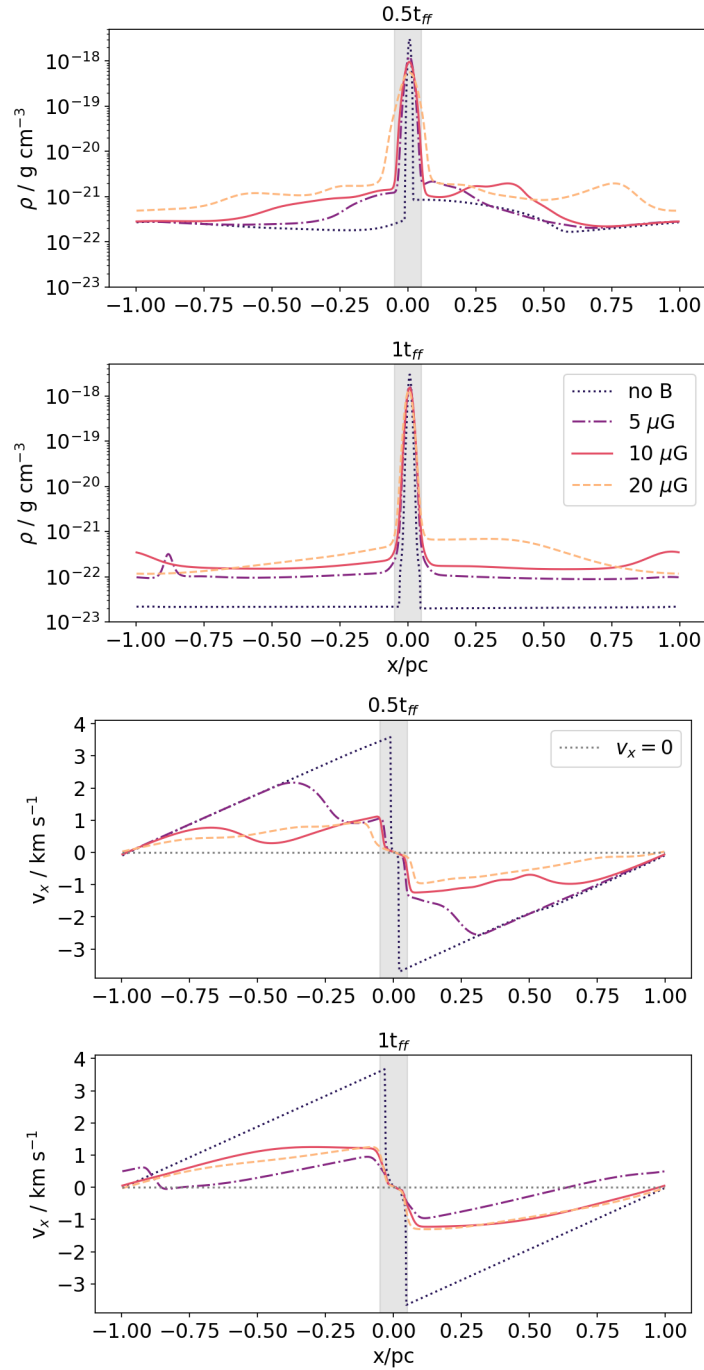
Figure 4.2.3: Density and velocity along the x-axis for the different initial magnitudes. The solid line correspond to the reference case. *Top panels*: $t = 0.5t_{\text{ff}}$; *bottom panels*: $t = 1.0t_{\text{ff}}$.
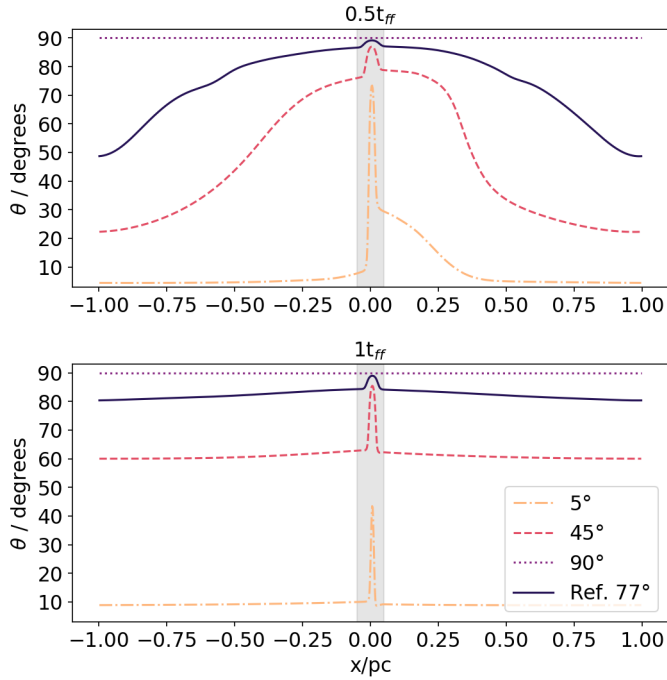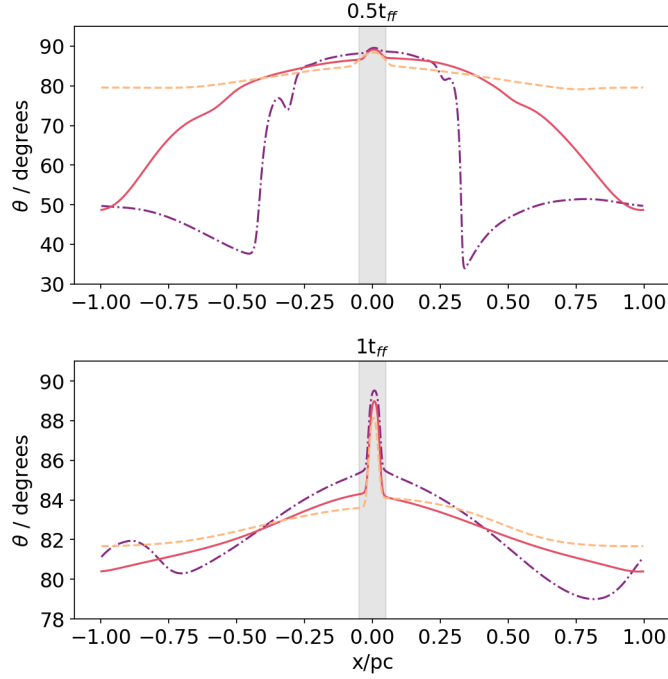
Figure 4.2.4: Inclination of the magnetic field for the different initial field strengths. The solid line correspond to the reference case. *Top panel*: $t = 0.5t_{\mathrm{ff}}$; *bottom panel*: $t = 1.0t_{\mathrm{ff}}$.

ideal behavior. Analogously, the density profile shows a broader distribution caused by a slow accretion towards the filament center, as shown in the right top panels of Fig. 4.3.1. This behavior is also confirmed by the velocity profile at 0.5 t_{ff}, that shows in the high CRIR case a shift of the v_x peak towards higher radii, determined by the relatively higher magnetic pressure support. This peak is no longer present at 1 t_{ff}, where the magnetic pressure halts the gravitational collapse, producing the slowest infall in the high CRIR case. By looking at the contribution of magnetic, thermal, and ram-pressure (Fig. 4.3.3), in general, the magnetic pressure is always dominant for each CRIR followed by ram-pressure. However, for the high ionization rate, the contribution of the magnetic pressure is remarkably high in the central region more than the ram and thermal pressures, but decreasing a little more for the ambient gas compared to the other CRIR. This shows the importance of the magnetic field for high ionization rates on the formation of the filament.
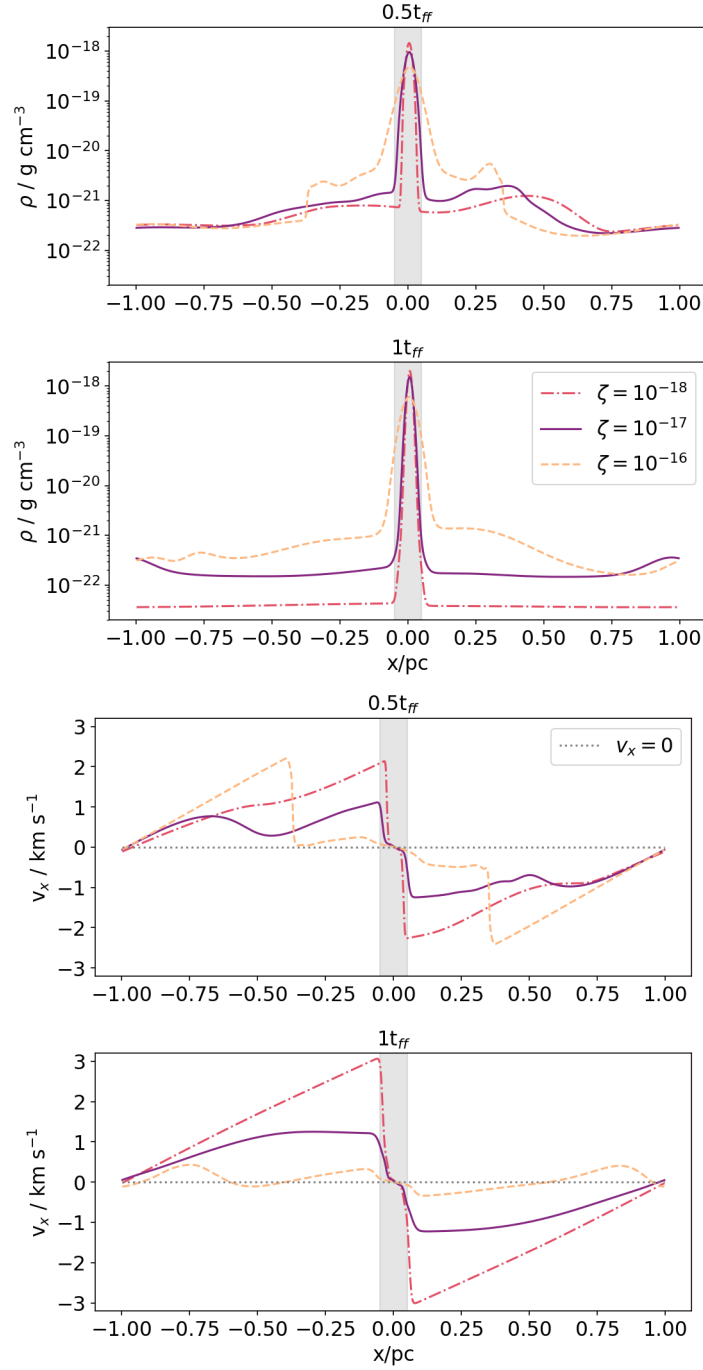
Figure 4.3.1: Density and velocity on the x-axis for different cosmic ray ionization rates. The black line correspond to the reference case. *Top panels*: $t = 0.5t_{\text{ff}}$; *bottom panels*: $t = 1.0t_{\text{ff}}$.
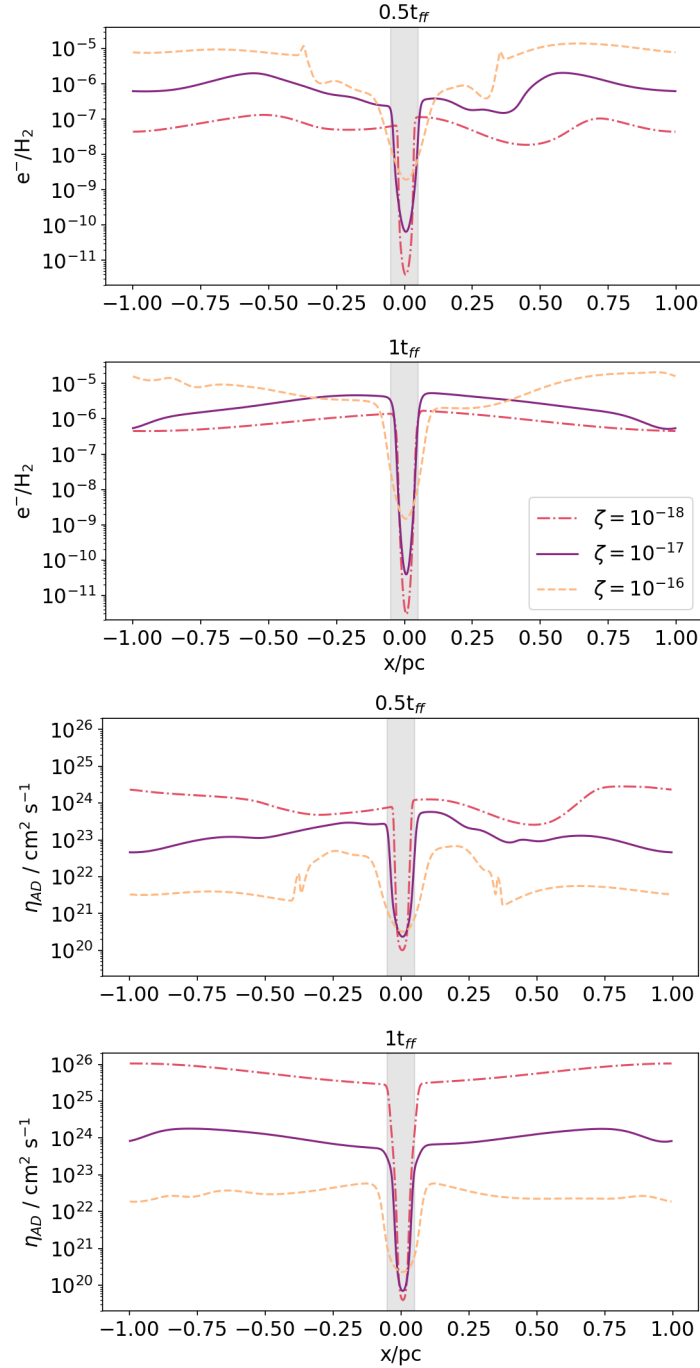
Figure 4.3.2: Ionization fraction and ambipolar diffusion resistivity coefficient for the different cosmic ray ionization rates. The black line correspond to the reference case. *Top panels*: $t = 0.5t_{\text{ff}}$; *bottom panels*: $t = 1.0t_{\text{ff}}$.
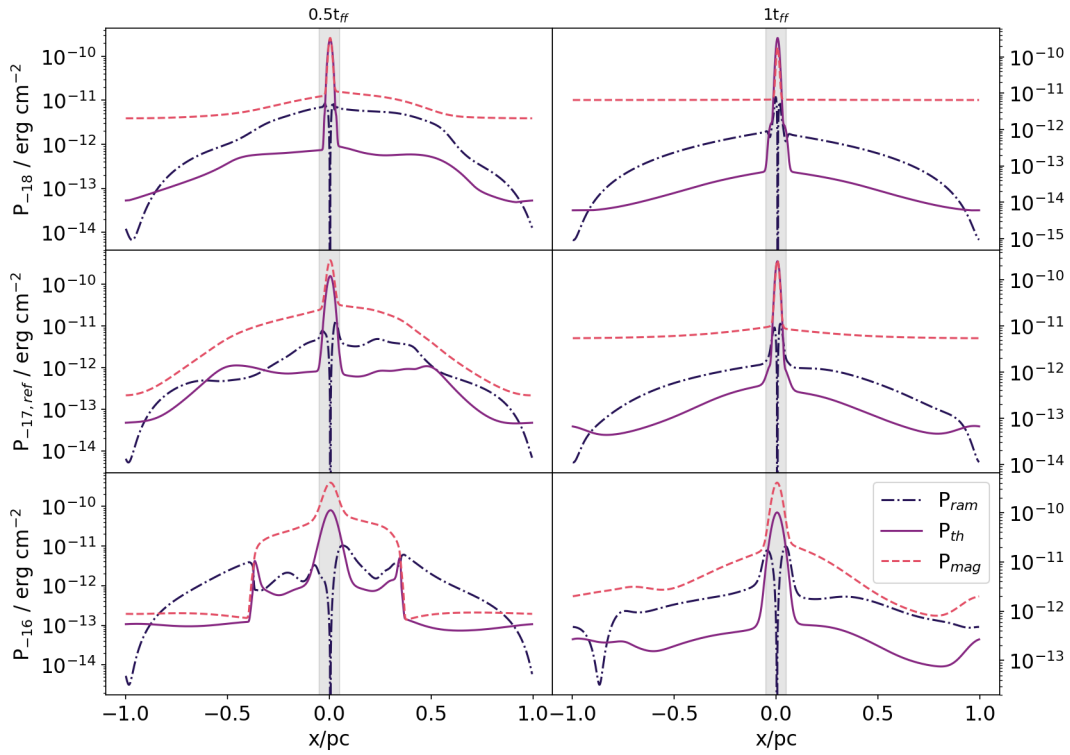
Figure 4.3.3: Comparison of ram, thermal and magnetic pressure for the different cosmic ray ionization rates. *Top panels*: low ionization rate (10^{-18} s^{-1}); *center panels*: reference case (10^{-17} s^{-1}); *bottom panels*: high ionization rate (10^{-16} s^{-1}). *Left panels*: $t = 0.5t_{\text{ff}}$; *Right panels*: $t = 1.0t_{\text{ff}}$.

4.4 Other parameters

To complete our analysis, we have studied the effect of additional parameters on the evolution of the filament. We have explored different initial Mach numbers, initial central density, the random seeds for the turbulence, and the exponent of the magnetic field – density relation, as in Eq. (3.2.8). By changing the initial turbulence seed we do not observe relevant differences in the final evolution of the filament, suggesting that in our case the global features are dominating over the local turbulence, that dissipates over time. In fact, the turbulence-induced fluctuations (e.g., Fig. 4.4.1 in the density profile) are more prominent at earlier stages. In the same way, for $\mathcal{M} = 4$ and 6, there is no significant change in the general evolution of different variables more than the typical fluctuations produced by the turbulent velocity at early stages.

For the different density regimes, we reduce ρ_{ridge} by factors of 0.1 and 0.5, where the free-fall time is recalculated due to the dependence on the density which make it increase for the reduced regimes, with $\sim$4.3 Myr and $\sim$1.9 Myr, respectively. As expected, at lower density becomes harder for the filament to form and to be distinguishable from the ambient gas even at the final stages, which can be attributed to the inability of the mass to provide sufficient gravity and contract the system magnetic fields. Similarly, reducing the density by a factor of 2 produces broader density profiles and a slower evolution (see Fig. 4.4.2). By changing the exponent of the magnetic field – density relation from $k = 0.5$ to $k = 0.4$, Eq. (3.2.8), the filament reaches higher temperatures, velocity, and central density, but almost the same density peak with respect to the reference, since the lower magnetic pressure cannot slow down the accretion efficiently. Conversely, for $k = 0.6$ (cf. 0.65 in Crutcher et al. 2010) the magnetic field is higher in both the ambient and the filament, and becomes more perpendicular to the flow compared to the previous cases, resulting in a slower accretion.

Though these parameters affect the global evolution, their effect is less pronounced than the effect of CRIR and of the initial magnetic field geometry.
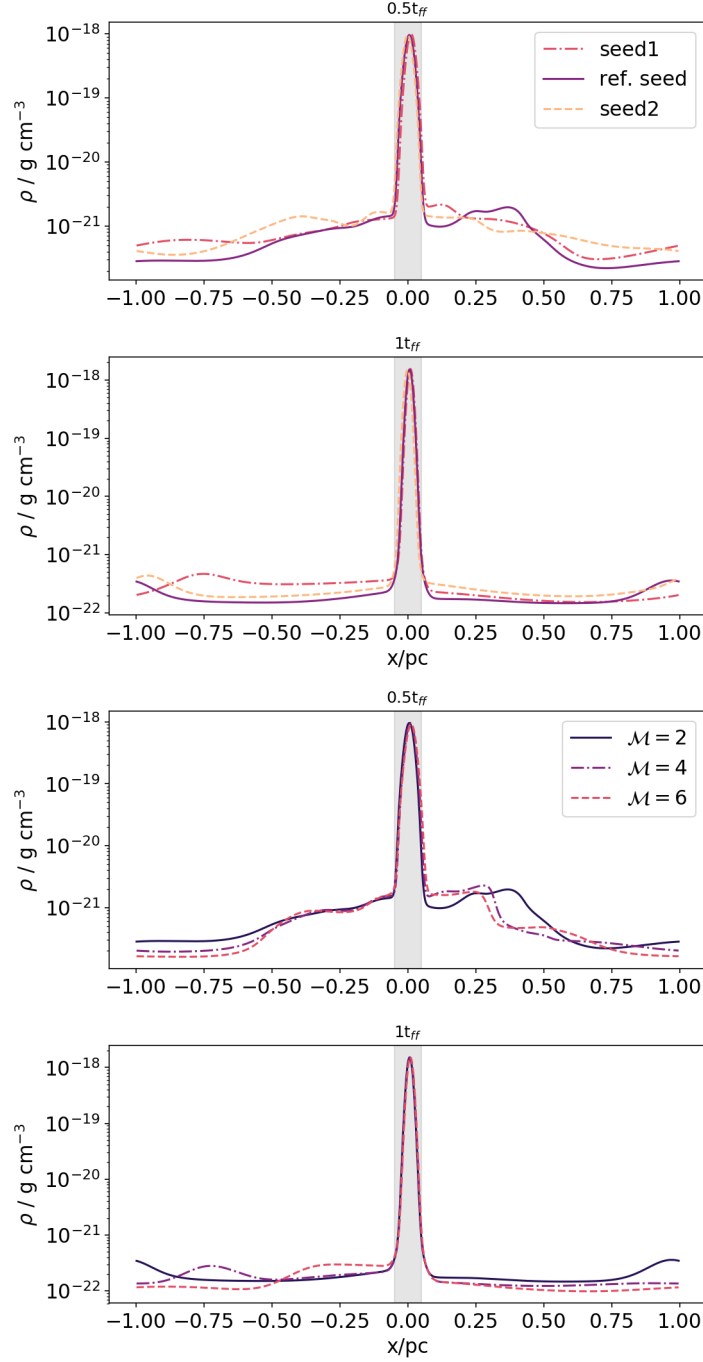
Figure 4.4.1: Density for different initial turbulence seeds and Mach number. The black line correspond to the reference case. *Top panels*: $t = 0.5t_{\mathrm{ff}}$; *bottom panels*: $t = 1.0t_{\mathrm{ff}}$.

Figure 4.4.2: Density for different initial central density and k-exponent of the magnetic field – density relation. The black line correspond to the reference case. *Top panels*: $t = 0.5t_{\mathrm{ff}}$; *bottom panels*: $t = 1.0t_{\mathrm{ff}}$.

Chapter 5

Discussion

In the previous sections, we observed how the different parameters affect the evolution of the filament, particularly the density and velocity, which are the main ingredients of the accretion mass flux. In the same way, by varying the density profiles leads to different shock positions, and hence widths. In this Section, we discuss the widths obtained from the shock positions, and the average accretion rate calculated at those positions.

To quantitatively assess the impact of the different parameters during the evolution of the gas, we define two global metrics: (i) the average accretion mass flux, $\langle \dot{\Sigma} \rangle$, and ($ii$) the Full-Width Half Maximum, FWHM, obtained by fitting the density profile with a Gaussian function including the background up to 0.1 pc (see e.g., Arzoumanian et al. 2011). The former is averaged over time, while the second is calculated at 1 t_{ff}.

In our case, we found that FWHM is a more suitable metric when compared to other methods, as for example the shock-tracking velocity divergence (cf. Priestley and Whitworth 2021). In fact, the find of the FWHM is directly controlled by the accretion, hence it is monotonically increasing with time, while the position of the shocks is a transient quantity that is designed to define the dynamical boundaries of the filament. A summary of these two metrics in terms of relative ratio with respect to the reference case is reported in Tab. 5.0.1, where in all the cases the accretion mass flux and the FHWM anticorrelates, since they are both controlled by the gas pressure support (either thermal and/or magnetic).

The largest effect is produced when assuming ideal MHD. In fact, the FHWM

	Ideal	$\theta = 5°$	$\theta = 45°$	$\theta = 90°$	no-B	$5\,\mu$G	$20\,\mu$G	$10^{-18}\,\mathrm{s}^{-1}$	$10^{-16}\,\mathrm{s}^{-1}$
$\frac{<\dot{\Sigma}>}{<\dot{\Sigma}_{\mathrm{ref}}>}$	0.410	1.372	1.366	0.960	1.684	1.663	0.919	1.317	0.706
$\frac{\mathrm{FWHM}}{\mathrm{FWHM}_{\mathrm{ref}}}$	7.214	0.575	0.698	1.046	0.534	0.922	1.159	0.755	2.447

Table 5.0.1: Time-averaged mass flux ratio, and FWHM ratio at $t = 1.0 t_{\mathrm{ff}}$, for ideal case, the different inclination angle, magnetic field strength, and cosmic rays ionization rate. Reference case have $\theta = 77°$, $B_0 = 10\,\mu$G, and $\zeta = 10^{-17}\,\mathrm{s}^{-1}$. Note that $\theta = 90°$ indicates that the magnetic field is perpendicular to the flow, and no-field corresponds to $B_0 = 0\,\mu$G.

is 7 times larger than the reference case, since the largest amount of magnetic pressure support reduces the accretion rate. For the same reason, the CRIR cases present an increased FWHM in the high-CRIR model, and vice versa for the low-CRIR. The magnetic pressure plays a crucial role also when changing the initial magnetic field; Reducing the field strength (no-B and $5\,\mu$G) narrows the density profile, while increasing the magnetic strength to $20\,\mu$G causes a relatively broader FWHM.

By changing the orientation of the initial magnetic field (θ) we observe a narrower FWHM when B_y tends to be parallel to the flow (i.e., θ=5°, almost perpendicular to the filament ridge). This decrease is driven by the magnitude of B_y, that is the only component that (by construction) varies spatially[1]. When θ is small B_x is the dominant component of the magnetic field, that is the component that, having no spatial gradient, plays a minor role in the MHD equations. In fact, in Fig. 4.2.1 right panels, v_x is larger for the smallest θ, being dominated by self-gravity, resulting in higher accretion and narrower FWHM.

To assess the impact of turbulence on the filament properties, we show in Fig. 5.0.1 the time evolution of the FWHM for different values of the Mach number, for the reference case. High Mach-number cases tend to behave similarly to $\mathcal{M} = 2$ except at earlier times when turbulence is dominant.

We define the edge of the filament using the divergence of the velocity, where we calculate the accretion mass flux (see Appendix B). In Fig. 5.0.2 we show the time evolution of the accretion mass flux in the reference model with ideal and non-ideal MHD. In general, the ideal case shows to be always lower than the

---

[1]B_z is also variable, but it is less relevant in this context, being always smaller than B_y. Moreover, B_z is expected to remain zero except for the fluctuations induced by turbulence, that produce a zero average of B_z.
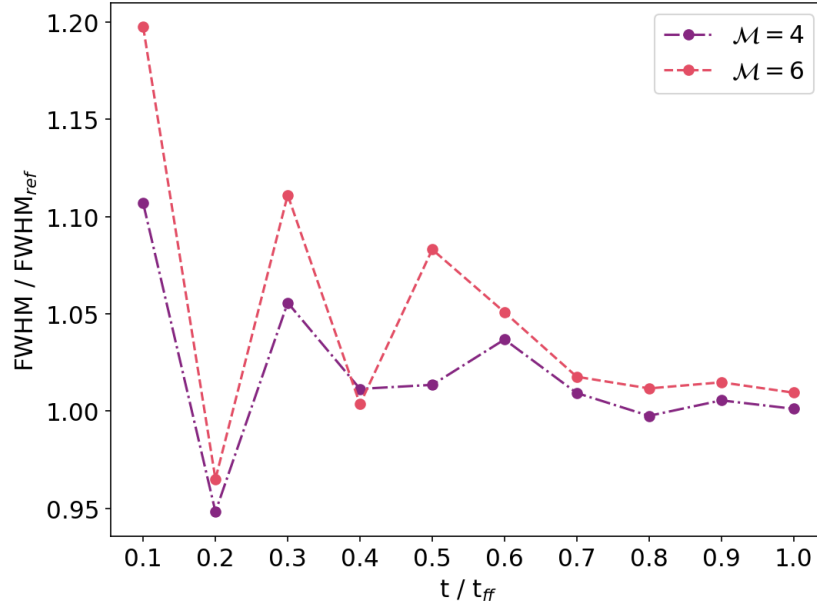
Figure 5.0.1: Time evolution of the FWHM ratio of $\mathcal{M} = 4$ (dot-dashed line) and $\mathcal{M} = 6$ (dashed line) with $\mathcal{M} = 2$ (reference).

non-ideal case, but for 0.2 and $0.5t_{\mathrm{ff}}$ shows similar values even higher. Anyway, after the half of the evolution both cases just decreases in time. This behavior is a result of the periodic boundary conditions: as the amount of mass in the box is limited, almost of the mass is accreted in the first stages.

To study the impact of the different parameters, we compare the accretion mass flux with the reference, as shows Table 5.0.1. In general, the accretion rates evolve from high values at early times (0.1–$0.4t_{\mathrm{ff}}$), decreasing from $0.5t_{\mathrm{ff}}$ to the final stages where the system almost stops accreting just as in the reference case. For the different configurations of the magnetic field, the *average* accretion rate is larger when θ is close to 45°. However, this behavior does not guarantee an efficient accretion with such configuration, this value is just an average of the accretion rate in all time steps. Indeed, from Section 4.2 it is clear that the configuration parallel to the flow is the most efficient for the accretion of material as it follows the direction of the flow, and configurations closer to 90° present higher accretion rates. A lower strength of the magnetic field makes the filament accrete more at the first stages, while for high strength, the accretion is more uniform with lower values at early times and higher ones at late times, but in general higher than in the case of low field strength. The unmagnetized case shows to be the higher case with respect to the reference, suggesting that the magnetic field provides to
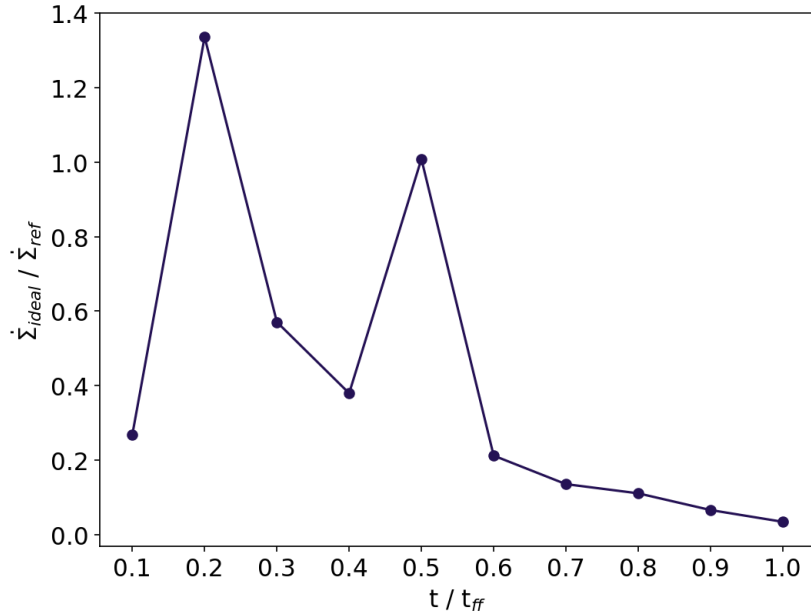
Figure 5.0.2: Time evolution of the accretion mass flux for ideal (dashed line) and non-ideal (solid line) MHD.

the mass transport to be accreted, and considering that for orientations parallel to the flow the accretion is more efficient, the field lines could be taking the role of transporting the mass, as proposed by Palmeirim et al. (2013). On the other hand, for higher cosmic-ray ionization rates, the accretion rate grows compared to the lower CRIR. This is due to the high CRIR case exhibiting a larger filament width, and higher densities at the shock position, whereas the opposite occurs in the low CRIR case.

Chapter 6

Limitations of the model

As in any numerical model, some approximations and assumptions need to be introduced in order to make the problem computationally tractable when including detailed microphysics, and when a parameter study is planned. The main limitation in our approach is the 1-D approximation employed to model the filament along the line of sight (x coordinate). Despite the code having three components for the vector variables, like velocity and magnetic field, the y and z coordinates (the diameter perpendicular to x and the component along the length of the filament) have periodic boundary conditions, that limit the exploration of the spatial variability. Additionally, in a 1-D code the solenoidal condition imposes by construction that the x component of the magnetic field is constant in time and space. Another set of periodic boundary conditions is imposed at the boundaries of the simulation domain to avoid infinitely growing accretion onto the filament (outflow boundaries), or nonphysical configurations (Dirichlet boundary conditions, i.e. zero derivatives). Ideally, this could be avoided by using a much larger simulation box, where the boundaries remain unaffected during the simulation due to their distance from the central filament ridge. However, such a set-up requires much more computational resources or an adaptive mesh, which is beyond the aims of the present work.

The microphysics is limited by the reduced set of chemical reactions, that however is capable of capturing the main features of larger chemical networks, especially the non-ideal behavior, as discussed in Grassi et al. (2019). In addition to this, since the chemistry has a noticeable influence on the cooling functions, the current

network might reduce the capability of our model to determine time-dependent effects of the thermal evolution. Finally, since the chemical network cannot be used to determine the ratio between the atomic and molecular species, we use a constant molecular weight and adiabatic index.

Additional limitations are discussed in Grassi et al. (2019), where the main features of the code are presented.

Chapter 7

Conclussion

In this one-dimensional study, we modeled an accreting self-gravitating turbulent filament using LEMONGRAB, a non-ideal MHD code that includes chemistry and microphysical processes. We explored how the main parameters, i.e., configuration and strengths of the magnetic field and cosmic ray ionization rate, and other parameters such as the Mach number, initial turbulence level, initial ridge density, and the exponent of the magnetic field – density relation affect the evolution and accretion of the filament. Our main results can be summarized as follows:

1. Including non-ideal MHD plays a crucial role for the filament evolution. The ideal case produces a wider filament, with a FWHM approximately seven times larger than the non-ideal model, due to the increased magnetic pressure support. This suggests that non-ideal MHD is fundamental to understand the accretion process.

2. Independently of the initial configuration of the magnetic field, the magnetic field lines in the central part of the filament bend to reach a perpendicular configuration with respect to the x-axis (i.e., the accretion direction). This is consistent, for example, with "U"-shaped model of Gómez et al. (2018).

3. Higher cosmic ray ionization rates produce higher ionization degrees that corresponds to a more ideal gas. As the coupling with the magnetic field is stronger, the magnetic pressure halts the collapse, resulting in a broader filament.

4. We do not find any strong change of the final FWHM with the Mach

number, pointing to a less pronounced role of the turbulence in regulating the evolution and the final properties of the filament compared to microphysics and the magnetic pressure. However, a one-dimensional model could be inadequate to address this specific question.

We conclude that adding magnetic fields and non-ideal MHD effects significantly affects the evolution of a collapsing filament, its width and its accretion rate, while other parameters play only a minor role. Special attention should be given to the cosmic ray ionization rate that strongly affect the coupling between the gas and the magnetic field. It is then fundamental to include in the future a proper cosmic rays propagation scheme to accurately study their effect on the accretion rate and on the filament width.

Bibliography

Alves de Oliveira, C., Schneider, N., Merín, B., Prusti, T., Ribas, Á., Cox, N. L. J., Vavrek, R., Könyves, V., Arzoumanian, D., Puga, E., Pilbratt, G. L., Kóspál, Á., André, P., Didelon, P., Men'shchikov, A., Royer, P., Waelkens, C., Bontemps, S., Winston, E., and Spezzi, L. (2014). Herschel view of the large-scale structure in the <ASTROBJ>Chamaeleon</ASTROBJ> dark clouds. *A&A*, 568:A98.

André, P., Di Francesco, J., Ward-Thompson, D., Inutsuka, S. I., Pudritz, R. E., and Pineda, J. E. (2014). From Filamentary Networks to Dense Cores in Molecular Clouds: Toward a New Paradigm for Star Formation. In Beuther, H., Klessen, R. S., Dullemond, C. P., and Henning, T., editors, *Protostars and Planets VI*, page 27.

André, P., Men'shchikov, A., Bontemps, S., Könyves, V., Motte, F., Schneider, N., Didelon, P., Minier, V., Saraceno, P., Ward-Thompson, D., di Francesco, J., White, G., Molinari, S., Testi, L., Abergel, A., Griffin, M., Henning, T., Royer, P., Merín, B., Vavrek, R., Attard, M., Arzoumanian, D., Wilson, C. D., Ade, P., Aussel, H., Baluteau, J. P., Benedettini, M., Bernard, J. P., Blommaert, J. A. D. L., Cambrésy, L., Cox, P., di Giorgio, A., Hargrave, P., Hennemann, M., Huang, M., Kirk, J., Krause, O., Launhardt, R., Leeks, S., Le Pennec, J., Li, J. Z., Martin, P. G., Maury, A., Olofsson, G., Omont, A., Peretto, N., Pezzuto, S., Prusti, T., Roussel, H., Russeil, D., Sauvage, M., Sibthorpe, B., Sicilia-Aguilar, A., Spinoglio, L., Waelkens, C., Woodcraft, A., and Zavagno, A. (2010). From filamentary clouds to prestellar cores to the stellar IMF: Initial highlights from the Herschel Gould Belt Survey. *A&A*, 518:L102.

André, P. (2017). Interstellar filaments and star formation. *Comptes Rendus Geoscience*, 349(5):187–197.

Arzoumanian, D., André, P., Didelon, P., Könyves, V., Schneider, N., Men'shchikov, A., Sousbie, T., Zavagno, A., Bontemps, S., di Francesco, J., Griffin, M., Hennemann, M., Hill, T., Kirk, J., Martin, P., Minier, V., Molinari, S., Motte, F., Peretto, N., Pezzuto, S., Spinoglio, L., Ward-Thompson, D., White, G., and Wilson, C. D. (2011). Characterizing interstellar filaments with Herschel in IC 5146. *A&A*, 529:L6.

Balsara, D., Ward-Thompson, D., and Crutcher, R. M. (2001). A turbulent MHD model for molecular clouds and a new method of accretion on to star-forming cores. *MNRAS*, 327(3):715–720.

Benedettini, M., Pezzuto, S., Schisano, E., André, P., Könyves, V., Men'shchikov, A., Ladjelate, B., Di Francesco, J., Elia, D., Arzoumanian, D., Louvet, F., Palmeirim, P., Rygl, K. L. J., Schneider, N., Spinoglio, L., and Ward-Thompson, D. (2018). A catalogue of dense cores and young stellar objects in the Lupus complex based on Herschel. Gould Belt Survey observations. *A&A*, 619:A52.

Bovino, S., Ferrada-Chamorro, S., Lupi, A., Sabatini, G., Giannetti, A., and Schleicher, D. R. G. (2019). The 3D Structure of CO Depletion in High-mass Prestellar Regions. *ApJ*, 887(2):224.

Bresnahan, D., Ward-Thompson, D., Kirk, J. M., Pattle, K., Eyres, S., White, G. J., Könyves, V., Men'shchikov, A., André, P., Schneider, N., Di Francesco, J., Arzoumanian, D., Benedettini, M., Ladjelate, B., Palmeirim, P., Bracco, A., Molinari, S., Pezzuto, S., and Spinoglio, L. (2018). The dense cores and filamentary structure of the molecular cloud in Corona Australis: Herschel SPIRE and PACS observations from the Herschel Gould Belt Survey. *A&A*, 615:A125.

Burkert, A. and Hartmann, L. (2004). Collapse and Fragmentation in Finite Sheets. *ApJ*, 616(1):288–300.

Chapman, N. L., Goldsmith, P. F., Pineda, J. L., Clemens, D. P., Li, D., and Krčo, M. (2011). The Magnetic Field in Taurus Probed by Infrared Polarization. *ApJ*, 741(1):21.

Cox, N. L. J., Arzoumanian, D., André, P., Rygl, K. L. J., Prusti, T., Men'shchikov, A., Royer, P., Kóspál, Á., Palmeirim, P., Ribas, A., Könyves, V., Bernard, J. P., Schneider, N., Bontemps, S., Merin, B., Vavrek, R., Alves de Oliveira, C., Didelon, P., Pilbratt, G. L., and Waelkens, C. (2016). Filamentary structure and magnetic field orientation in Musca. *A&A*, 590:A110.

Crutcher, R. M. (2012). Magnetic fields in molecular clouds. *Annual Review of Astronomy and Astrophysics*, 50(1):29–63.

Crutcher, R. M., Wandelt, B., Heiles, C., Falgarone, E., and Troland, T. H. (2010). Magnetic Fields in Interstellar Clouds from Zeeman Observations: Inference of Total Field Strengths by Bayesian Analysis. *ApJ*, 725(1):466–479.

Draine, B. T., Roberge, W. G., and Dalgarno, A. (1983). Magnetohydrodynamic shock waves in molecular clouds. *ApJ*, 264:485–507.

Evans II, N. J. (1999). Physical conditions in regions of star formation. *Annual Review of Astronomy and Astrophysics*, 37(1):311–362.

Ferland, G. J., Korista, K. T., Verner, D. A., Ferguson, J. W., Kingdon, J. B., and Verner, E. M. (1998). CLOUDY 90: Numerical Simulation of Plasmas and Their Spectra. *PASP*, 110(749):761–778.

Fujii, Y. I., Okuzumi, S., and Inutsuka, S.-i. (2011). A Fast and Accurate Calculation Scheme for Ionization Degrees in Protoplanetary and Circumplanetary Disks with Charged Dust Grains. *ApJ*, 743(1):53.

Fukui, Y. and Kawamura, A. (2010). Molecular clouds in nearby galaxies. *Annual Review of Astronomy and Astrophysics*, 48(1):547–580.

Galli, D. and Padovani, M. (2015). Cosmic-ray heating of molecular cloud cores. *arXiv e-prints*, page arXiv:1502.03380.

Gómez, G. C. and Vázquez-Semadeni, E. (2014). Filaments in Simulations of Molecular Cloud Formation. *ApJ*, 791(2):124.

Gómez, G. C., Vázquez-Semadeni, E., and Zamora-Avilés, M. (2018). The magnetic field structure in molecular cloud filaments. *MNRAS*, 480(3):2939–2944.

Grassi, T., Padovani, M., Ramsey, J. P., Galli, D., Vaytet, N., Ercolano, B., and Haugbølle, T. (2019). The challenges of modelling microphysics: ambipolar diffusion, chemistry, and cosmic rays in MHD shocks. *MNRAS*, 484(1):161–184.

Hartmann, L. (2009). *Accretion Processes in Star Formation: Second Edition*.

Heiles, C. (2000). The Magnetic Field in the Milky Way Galaxy. In *APS April Meeting Abstracts*, page B7.003.

Hennebelle, P. and André, P. (2013). Ion-neutral friction and accretion-driven turbulence in self-gravitating filaments. *A&A*, 560:A68.

Hennebelle, P. and Audit, E. (2008). Structure of the turbulent atomic gas and formation of molecular clouds. In Kramer, C., Aalto, S., and Simon, R., editors, *EAS Publications Series*, volume 31 of *EAS Publications Series*, pages 15–18.

Hennebelle, P. and Inutsuka, S.-i. (2019). The role of magnetic field in molecular cloud formation and evolution. *arXiv e-prints*, page arXiv:1902.00798.

Heyer, M. and Dame, T. (2015). Molecular clouds in the milky way. *Annual Review of Astronomy and Astrophysics*, 53(1):583–629.

Heyer, M., Gong, H., Ostriker, E., and Brunt, C. (2008). Magnetically Aligned Velocity Anisotropy in the Taurus Molecular Cloud. *ApJ*, 680(1):420–427.

Inoue, T. and ichiro Inutsuka, S. (2012). Formation of turbulent and magnetized molecular clouds via accretion flows of h i clouds. *The Astrophysical Journal*, 759:35.

Inoue, T., Inutsuka, S.-i., and Koyama, H. (2007). The Role of Ambipolar Diffusion in the Formation Process of Moderately Magnetized Diffuse Clouds. *ApJL*, 658(2):L99–L102.

Kirk, H., Klassen, M., Pudritz, R., and Pillsworth, S. (2015). The Role of Turbulence and Magnetic Fields in Simulated Filamentary Structure. *ApJ*, 802(2):75.

Kirk, J. M., Ward-Thompson, D., Palmeirim, P., André, P., Griffin, M. J., Hargrave, P. J., Könyves, V., Bernard, J.-P., Nutter, D. J., Sibthorpe, B., Di Francesco, J., Abergel, A., Arzoumanian, D., Benedettini, M., Bontemps,

S., Elia, D., Hennemann, M., Hill, T., Men'shchikov, A., Motte, F., Nguyen-Luong, Q., Peretto, N., Pezzuto, S., Rygl, K. L. J., Sadavoy, S. I., Schisano, E., Schneider, N., Testi, L., and White, G. (2013). First results from the Herschel Gould Belt Survey in Taurus. *MNRAS*, 432(2):1424–1433.

Könyves, V., André, P., Men'shchikov, A., Palmeirim, P., Arzoumanian, D., Schneider, N., Roy, A., Didelon, P., Maury, A., Shimajiri, Y., Di Francesco, J., Bontemps, S., Peretto, N., Benedettini, M., Bernard, J. P., Elia, D., Griffin, M. J., Hill, T., Kirk, J., Ladjelate, B., Marsh, K., Martin, P. G., Motte, F., Nguyên Luong, Q., Pezzuto, S., Roussel, H., Rygl, K. L. J., Sadavoy, S. I., Schisano, E., Spinoglio, L., Ward-Thompson, D., and White, G. J. (2015). A census of dense cores in the Aquila cloud complex: SPIRE/PACS observations from the Herschel Gould Belt survey. *A&A*, 584:A91.

Körtgen, B., Bovino, S., Schleicher, D. R. G., Giannetti, A., and Banerjee, R. (2017). Deuterium fractionation and H_2D^+ evolution in turbulent and magnetized cloud cores. *MNRAS*, 469(3):2602–2625.

Körtgen, B., Bovino, S., Schleicher, D. R. G., Stutz, A., Banerjee, R., Giannetti, A., and Leurini, S. (2018). Fast deuterium fractionation in magnetized and turbulent filaments. *MNRAS*, 478(1):95–109.

Krumholz, M. R. (2015). Notes on Star Formation. *arXiv e-prints*, page arXiv:1511.03457.

Lequeux, J. (2005). *The Interstellar Medium*.

Marchand, P., Masson, J., Chabrier, G., Hennebelle, P., Commerçon, B., and Vaytet, N. (2016). Chemical solver to compute molecule and grain abundances and non-ideal MHD resistivities in prestellar core-collapse calculations. *A&A*, 592:A18.

Masson, J., Teyssier, R., Mulet-Marquis, C., Hennebelle, P., and Chabrier, G. (2012). Incorporating Ambipolar and Ohmic Diffusion in the AMR MHD Code RAMSES. *ApJS*, 201(2):24.

Mathis, J. S., Rumpl, W., and Nordsieck, K. H. (1977). The size distribution of interstellar grains. *ApJ*, 217:425–433.

Molinari, S., Swinyard, B., Bally, J., Barlow, M., Bernard, J. P., Martin, P., Moore, T., Noriega-Crespo, A., Plume, R., Testi, L., Zavagno, A., Abergel, A., Ali, B., Anderson, L., André, P., Baluteau, J. P., Battersby, C., Beltrán, M. T., Benedettini, M., Billot, N., Blommaert, J., Bontemps, S., Boulanger, F., Brand, J., Brunt, C., Burton, M., Calzoletti, L., Carey, S., Caselli, P., Cesaroni, R., Cernicharo, J., Chakrabarti, S., Chrysostomou, A., Cohen, M., Compiegne, M., de Bernardis, P., de Gasperis, G., di Giorgio, A. M., Elia, D., Faustini, F., Flagey, N., Fukui, Y., Fuller, G. A., Ganga, K., Garcia-Lario, P., Glenn, J., Goldsmith, P. F., Griffin, M., Hoare, M., Huang, M., Ikhenaode, D., Joblin, C., Joncas, G., Juvela, M., Kirk, J. M., Lagache, G., Li, J. Z., Lim, T. L., Lord, S. D., Marengo, M., Marshall, D. J., Masi, S., Massi, F., Matsuura, M., Minier,

V., Miville-Deschênes, M. A., Montier, L. A., Morgan, L., Motte, F., Mottram, J. C., Müller, T. G., Natoli, P., Neves, J., Olmi, L., Paladini, R., Paradis, D., Parsons, H., Peretto, N., Pestalozzi, M., Pezzuto, S., Piacentini, F., Piazzo, L., Polychroni, D., Pomarès, M., Popescu, C. C., Reach, W. T., Ristorcelli, I., Robitaille, J. F., Robitaille, T., Rodón, J. A., Roy, A., Royer, P., Russeil, D., Saraceno, P., Sauvage, M., Schilke, P., Schisano, E., Schneider, N., Schuller, F., Schulz, B., Sibthorpe, B., Smith, H. A., Smith, M. D., Spinoglio, L., Stamatellos, D., Strafella, F., Stringfellow, G. S., Sturm, E., Taylor, R., Thompson, M. A., Traficante, A., Tuffs, R. J., Umana, G., Valenziano, L., Vavrek, R., Veneziani, M., Viti, S., Waelkens, C., Ward-Thompson, D., White, G., Wilcock, L. A., Wyrowski, F., Yorke, H. W., and Zhang, Q. (2010). Clouds, filaments, and protostars: The Herschel Hi-GAL Milky Way. *A&A*, 518:L100.

Nakamura, F. and Li, Z.-Y. (2008). Magnetically Regulated Star Formation in Three Dimensions: The Case of the Taurus Molecular Cloud Complex. *ApJ*, 687(1):354–375.

Padoan, P. and Nordlund, A. (1997). Supersonic motions in dark clouds are not Alfven waves. *arXiv e-prints*, pages astro–ph/9706176.

Padovani, M. and Galli, D. (2011). Effects of magnetic fields on the cosmic-ray ionization of molecular cloud cores. *A&A*, 530:A109.

Padovani, M., Galli, D., and Glassgold, A. E. (2009). Cosmic-ray ionization of molecular clouds. *A&A*, 501(2):619–631.

Palmeirim, P., André, P., Kirk, J., Ward-Thompson, D., Arzoumanian, D., Könyves, V., Didelon, P., Schneider, N., Benedettini, M., Bontemps, S., Di Francesco, J., Elia, D., Griffin, M., Hennemann, M., Hill, T., Martin, P. G., Men'shchikov, A., Molinari, S., Motte, F., Nguyen Luong, Q., Nutter, D., Peretto, N., Pezzuto, S., Roy, A., Rygl, K. L. J., Spinoglio, L., and White, G. L. (2013). Herschel view of the Taurus B211/3 filament and striations: evidence of filamentary growth? *A&A*, 550:A38.

Panopoulou, G., Clark, S., Hacar, A., Heitsch, F., Kainulainen, J., Ntormousi, E., Seifried, D., and Smith, R. (2021). The width of herschel filaments varies with distance. *Astronomy & Astrophysics*.

Planck Collaboration, Adam, R., Ade, P. A. R., Aghanim, N., Alves, M. I. R., Arnaud, M., Arzoumanian, D., Ashdown, M., Aumont, J., Baccigalupi, C., Banday, A. J., Barreiro, R. B., Bartolo, N., Battaner, E., Benabed, K., Benoit-Lévy, A., Bernard, J. P., Bersanelli, M., Bielewicz, P., Bonaldi, A., Bonavera, L., Bond, J. R., Borrill, J., Bouchet, F. R., Boulanger, F., Bracco, A., Burigana, C., Butler, R. C., Calabrese, E., Cardoso, J. F., Catalano, A., Chamballu, A., Chiang, H. C., Christensen, P. R., Colombi, S., Colombo, L. P. L., Combet, C., Couchot, F., Crill, B. P., Curto, A., Cuttaia, F., Danese, L., Davies, R. D., Davis, R. J., de Bernardis, P., de Rosa, A., de Zotti, G., Delabrouille, J., Dickinson, C., Diego, J. M., Dole, H., Donzelli, S., Doré, O., Douspis, M., Ducout, A., Dupac, X., Efstathiou, G., Elsner, F., Enßlin, T. A., Eriksen, H. K.,

Falgarone, E., Ferrière, K., Finelli, F., Forni, O., Frailis, M., Fraisse, A. A., Franceschi, E., Frejsel, A., Galeotta, S., Galli, S., Ganga, K., Ghosh, T., Giard, M., Gjerløw, E., González-Nuevo, J., Górski, K. M., Gregorio, A., Gruppuso, A., Guillet, V., Hansen, F. K., Hanson, D., Harrison, D. L., Henrot-Versillé, S., Hernández-Monteagudo, C., Herranz, D., Hildebrandt, S. R., Hivon, E., Hobson, M., Holmes, W. A., Hovest, W., Huffenberger, K. M., Hurier, G., Jaffe, A. H., Jaffe, T. R., Jones, W. C., Juvela, M., Keihänen, E., Keskitalo, R., Kisner, T. S., Kneissl, R., Knoche, J., Kunz, M., Kurki-Suonio, H., Lagache, G., Lamarre, J. M., Lasenby, A., Lattanzi, M., Lawrence, C. R., Leonardi, R., Levrier, F., Liguori, M., Lilje, P. B., Linden-Vørnle, M., López-Caniego, M., Lubin, P. M., Macías-Pérez, J. F., Maffei, B., Maino, D., Mandolesi, N., Maris, M., Marshall, D. J., Martin, P. G., Martínez-González, E., Masi, S., Matarrese, S., Mazzotta, P., Melchiorri, A., Mendes, L., Mennella, A., Migliaccio, M., Miville-Deschênes, M. A., Moneti, A., Montier, L., Morgante, G., Mortlock, D., Munshi, D., Murphy, J. A., Naselsky, P., Natoli, P., Nørgaard-Nielsen, H. U., Noviello, F., Novikov, D., Novikov, I., Oppermann, N., Oxborrow, C. A., Pagano, L., Pajot, F., Paoletti, D., Pasian, F., Perdereau, O., Perotto, L., Perrotta, F., Pettorino, V., Piacentini, F., Piat, M., Plaszczynski, S., Pointecouteau, E., Polenta, G., Ponthieu, N., Popa, L., Pratt, G. W., Prunet, S., Puget, J. L., Rachen, J. P., Reach, W. T., Reinecke, M., Remazeilles, M., Renault, C., Ristorcelli, I., Rocha, G., Roudier, G., Rubiño-Martín, J. A., Rusholme, B., Sandri, M., Santos, D., Savini, G., Scott, D., Soler, J. D., Spencer, L. D., Stolyarov, V., Sudiwala, R., Sunyaev, R., Sutton, D., Suur-Uski, A. S., Sygnet, J. F., Tauber, J. A., Terenzi, L., Toffolatti, L., Tomasi, M., Tristram, M., Tucci, M., Umana, G., Valenziano, L., Valiviita, J., Van Tent, B., Vielva, P., Villa, F., Wade, L. A., Wandelt, B. D., Wehus, I. K., Wiesemeyer, H., Yvon, D., Zacchei, A., and Zonca, A. (2016a). Planck intermediate results. XXXII. The relative orientation between the magnetic field and structures traced by interstellar dust. *A&A*, 586:A135.

Planck Collaboration, Ade, P. A. R., Aghanim, N., Alves, M. I. R., Arnaud, M., Arzoumanian, D., Aumont, J., Baccigalupi, C., Banday, A. J., Barreiro, R. B., Bartolo, N., Battaner, E., Benabed, K., Benoit-Lévy, A., Bernard, J. P., Berné, O., Bersanelli, M., Bielewicz, P., Bonaldi, A., Bonavera, L., Bond, J. R., Borrill, J., Bouchet, F. R., Boulanger, F., Bracco, A., Burigana, C., Calabrese, E., Cardoso, J. F., Catalano, A., Chamballu, A., Chiang, H. C., Christensen, P. R., Clements, D. L., Colombi, S., Colombo, L. P. L., Combet, C., Couchot, F., Crill, B. P., Curto, A., Cuttaia, F., Danese, L., Davies, R. D., Davis, R. J., de Bernardis, P., de Rosa, A., de Zotti, G., Delabrouille, J., Dickinson, C., Diego, J. M., Donzelli, S., Doré, O., Douspis, M., Ducout, A., Dupac, X., Elsner, F., Enßlin, T. A., Eriksen, H. K., Falgarone, E., Ferrière, K., Finelli, F., Forni, O., Frailis, M., Fraisse, A. A., Franceschi, E., Frejsel, A., Galeotta, S., Galli, S., Ganga, K., Ghosh, T., Giard, M., Giraud-Héraud, Y., Gjerløw, E., González-Nuevo, J., Górski, K. M., Gregorio, A., Gruppuso, A., Guillet, V., Hansen, F. K., Hanson, D., Harrison, D. L., Hernández-Monteagudo, C., Herranz, D., Hildebrandt, S. R., Hivon, E., Hobson, M., Holmes, W. A., Huffenberger, K. M., Hurier, G., Jaffe, A. H., Jaffe, T. R., Jones, W. C., Juvela, M., Keskitalo, R.,

Kisner, T. S., Knoche, J., Kunz, M., Kurki-Suonio, H., Lagache, G., Lamarre, J. M., Lasenby, A., Lawrence, C. R., Leonardi, R., Levrier, F., Liguori, M., Lilje, P. B., Linden-Vørnle, M., López-Caniego, M., Lubin, P. M., Macías-Pérez, J. F., Maffei, B., Mandolesi, N., Mangilli, A., Maris, M., Martin, P. G., Martínez-González, E., Masi, S., Matarrese, S., Mazzotta, P., Melchiorri, A., Mendes, L., Mennella, A., Migliaccio, M., Mitra, S., Miville-Deschênes, M. A., Moneti, A., Montier, L., Morgante, G., Mortlock, D., Munshi, D., Murphy, J. A., Naselsky, P., Nati, F., Natoli, P., Nørgaard-Nielsen, H. U., Noviello, F., Novikov, D., Novikov, I., Oppermann, N., Pagano, L., Pajot, F., Paladini, R., Paoletti, D., Pasian, F., Perrotta, F., Pettorino, V., Piacentini, F., Piat, M., Pierpaoli, E., Pietrobon, D., Plaszczynski, S., Pointecouteau, E., Polenta, G., Pratt, G. W., Puget, J. L., Rachen, J. P., Rebolo, R., Reinecke, M., Remazeilles, M., Renault, C., Renzi, A., Ricciardi, S., Ristorcelli, I., Rocha, G., Rosset, C., Rossetti, M., Roudier, G., Rubiño-Martín, J. A., Rusholme, B., Sandri, M., Savelainen, M., Savini, G., Scott, D., Soler, J. D., Stolyarov, V., Sutton, D., Suur-Uski, A. S., Sygnet, J. F., Tauber, J. A., Terenzi, L., Toffolatti, L., Tomasi, M., Tristram, M., Tucci, M., Valenziano, L., Valiviita, J., Van Tent, B., Vielva, P., Villa, F., Wade, L. A., Wandelt, B. D., Yvon, D., Zacchei, A., and Zonca, A. (2016b). Planck intermediate results. XXXIII. Signature of the magnetic field geometry of interstellar filaments in dust polarization maps. *A&A*, 586:A136.

Priestley, F. D. and Whitworth, A. P. (2021). The origin of a universal filament width in molecular clouds. *MNRAS*.

Schneider, N., Csengeri, T., Bontemps, S., Motte, F., Simon, R., Hennebelle, P., Federrath, C., and Klessen, R. (2010). Dynamic star formation in the massive DR21 filament. *A&A*, 520:A49.

Seifried, D. and Walch, S. (2015). The impact of turbulence and magnetic field orientation on star-forming filaments. *MNRAS*, 452(3):2410–2422.

Shen, S., Madau, P., Guedes, J., Mayer, L., Prochaska, J. X., and Wadsley, J. (2013). The Circumgalactic Medium of Massive Galaxies at z ~3: A Test for Stellar Feedback, Galactic Outflows, and Cold Streams. *ApJ*, 765(2):89.

Shimajiri, Y., André, P., Palmeirim, P., Arzoumanian, D., Bracco, A., Könyves, V., Ntormousi, E., and Ladjelate, B. (2019). Probing accretion of ambient cloud material into the Taurus B211/B213 filament. *A&A*, 623:A16.

Shu, F. H. (1983). Ambipolar diffusion in self-gravitating isothermal layers. *ApJ*, 273:202–213.

Shu, F. H. (1992). Books-Received - the Physics of Astrophysics - V.2 - Gas Dynamics. *Journal of the British Astronomical Association*, 102:230.

Soler, J. D., Hennebelle, P., Martin, P. G., Miville-Deschênes, M. A., Netterfield, C. B., and Fissel, L. M. (2013). An Imprint of Molecular Cloud Magnetization in the Morphology of the Dust Polarized Emission. *ApJ*, 774(2):128.

Tilley, D. A. and Pudritz, R. E. (2007). The formation of star clusters - II. 3D

simulations of magnetohydrodynamic turbulence in molecular clouds. *MNRAS*, 382(1):73–94.

Ward-Thompson, D., Kirk, J. M., André, P., Saraceno, P., Didelon, P., Könyves, V., Schneider, N., Abergel, A., Baluteau, J. P., Bernard, J. P., Bontemps, S., Cambrésy, L., Cox, P., di Francesco, J., di Giorgio, A. M., Griffin, M., Hargrave, P., Huang, M., Li, J. Z., Martin, P., Men'shchikov, A., Minier, V., Molinari, S., Motte, F., Olofsson, G., Pezzuto, S., Russeil, D., Sauvage, M., Sibthorpe, B., Spinoglio, L., Testi, L., White, G., Wilson, C., Woodcraft, A., and Zavagno, A. (2010). A Herschel study of the properties of starless cores in the Polaris Flare dark cloud region using PACS and SPIRE. *A&A*, 518:L92.

Wardle, M. (2007). Magnetic fields in protoplanetary disks. *Ap&SS*, 311(1-3):35–45.

Xu, S., Ji, S., and Lazarian, A. (2019). On the formation of density filaments in the turbulent interstellar medium. *arXiv e-prints*, page arXiv:1905.06341.

Appendix A

Resolution test

To test if our results are affected by the resolution used in the code, we test different number of cells as 246, 548, and 1024 with the same 2 pc box-size. By looking at the most important quantities, we can see that the resolution does not alter the results. Here we show the density (one of the most showed quantity in this work) in Fig. A0.1 at the initial conditions, $0.3t_{\mathrm{ff}}$, $0.7t_{\mathrm{ff}}$ and $1t_{\mathrm{ff}}$.
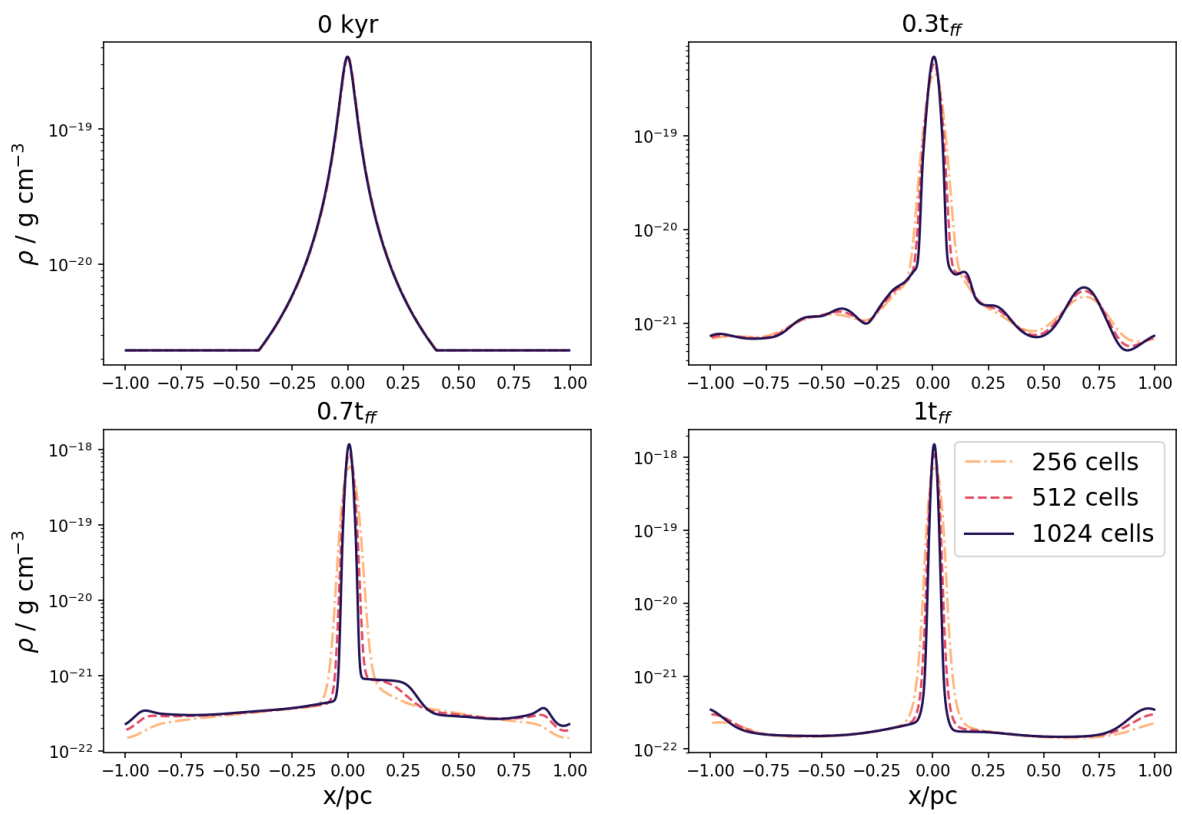
Figure A0.1: Density for different resolutions with 246 (dotted-dashed line), 512 (dashed line) and 1024 (continuous line) cells at the initial conditions, 0.3, 0.7 and $1t_{\mathrm{ff}}$.

Appendix B

Boundaries of the filament

As there is no unique definition of the boundaries of a filament, we calculate the mass flux for the reference case at different distances from the filament axis to compare with the observational data. These positions are given by: (a) the minimum values of the velocity-divergence (or x-velocity gradient); (b) $x = \pm 0.05$ pc from the axis of the filament (half of the typical observed width); (c) the distance where the enclosed mass is 80% of the total mass in the computational box; and (d) where the flow becomes supersonic with a possible shock with Mach number $\mathcal{M} = 1$. Fig. A0.1 shows the evolution of the mass fluxes in each time-step for each case, where dots correspond to non-ideal MHD and stars to ideal MHD. By looking at the ideal case (stars) we note that the difference is not very large after $0.3 t_{\mathrm{ff}}$. The total averaged mass fluxes in time for non-ideal MHD are 206.15 $\mathrm{M}_\odot \, \mathrm{Myr}^{-1} \, \mathrm{pc}^{-2}$ for the criterion (a); 194.02 $\mathrm{M}_\odot \, \mathrm{Myr}^{-1} \, \mathrm{pc}^{-2}$ for the criterion (b); 715.87 $\mathrm{M}_\odot \, \mathrm{Myr}^{-1} \, \mathrm{pc}^{-2}$ for the criterion (c); and 438.38 $\mathrm{M}_\odot \, \mathrm{Myr}^{-1} \, \mathrm{pc}^{-2}$ for $\mathcal{M} = 1$ for the criterion (d).

Observational studies such as Palmeirim et al. (2013) provided an estimate of the accretion rate in the B211 filament based on the observed mass per unit length and the $^{12}\mathrm{CO}$ (1–0) inflow velocity, finding a value of $\sim$ 27–50 $\mathrm{M}_\odot \, \mathrm{Myr}^{-1} \, \mathrm{pc}^{-1}$. With this accretion rate, it would take $\sim$ 1–2 Myr to form the B211 filament, in reasonable agreement with the free-fall time of $\sim$ 1.3 Myr of our model. Since the accretion rate is estimated in the observations at a distance of 0.4 pc from the filament axis, the method of the width is not appropriate for a comparison, because of the smaller radius used and because the width of the filament changes
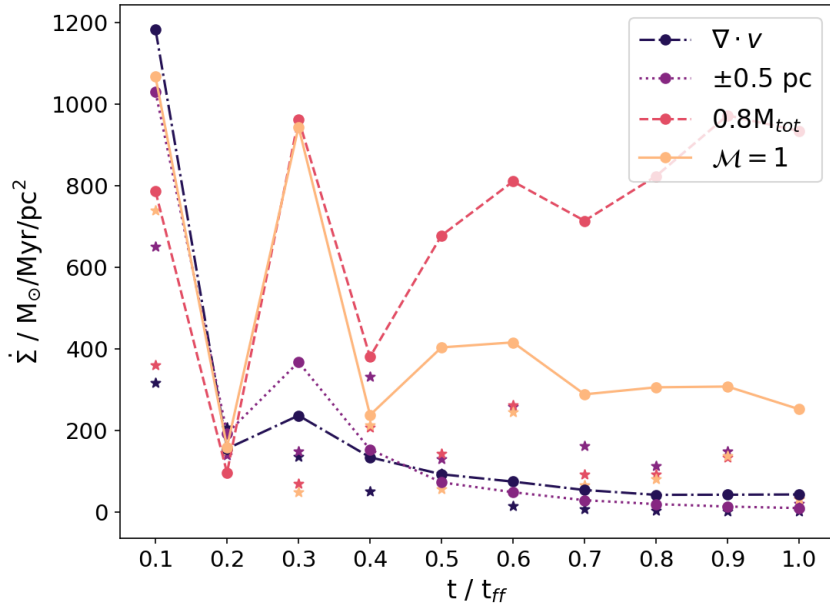
Figure A0.1: Time evolution of the mass flux according to the different methods adopted here. Circles correspond to non-ideal MHD, stars to ideal MHD.

with time. The methods based on Mach number and $0.8M_{\text{tot}}$ are not well suited for a comparison, as they assume a position too close to the filament center. On the other hand, the method of the velocity-divergence shows more similarity with the observations, where the inflow velocity is ~ 0.6–1.1 km s^{-1} while in our model the velocity in the x-axis at the free-fall time $t = t_{\text{ff}}$ is ~ 1.2 km s^{-1} at ~ 0.1 pc from the center of the filament.